

CANCER

Targeting the origins of multiple myeloma along hematopoietic stem cell lymphoid lineage differentiation

Jiaojiao Guo^{1,2†}, Yaru Li^{3†}, Zhiling Yan^{4†}, Qing Li^{5†}, Zhenhao Liu⁶, Zhengjiang Li¹, Ruiqi Zhou¹, Nihai He¹, Yinghong Zhu¹, Xiaoshuang Wang⁷, Xun Chen², Yi Qiu¹, Liang Zhao¹, Fangming Shi², Yanjuan He¹, Sha Hao⁵, Jia Yu⁷, Lu Xie⁶, Jiaxi Zhou⁵, Jian Li⁸, Gang An⁵, Xiangling Feng⁹, Wei Jia¹⁰, Xiaochen Bo³, Kailin Xu^{4*}, Tao Cheng^{5*}, Hebing Chen^{3*}, Wen Zhou^{1,2*}

Copyright © 2025 The Authors, some rights reserved; exclusive licensee American Association for the Advancement of Science. No claim to original U.S. Government Works

The initiation and progression of multiple myeloma (MM) are intricate processes, and a critical challenge lies in understanding the mechanisms of malignant transformation in MM-initiating cells (MICs) and their driver genes. In this study, we used single-cell sequencing and genetic tracer analysis at each developmental stage, from hematopoietic stem cells to lymphoid lineage differentiation, to identify abnormal differentiation stages in patients with MM. We found that chromosome 1q amplification (1q^{Amp}) originated from a specific subgroup of B cells, whereas chromosome 17p deletion occurred at the plasma cell stage. 1q^{Amp} was present in CD24⁻FCRL5⁺ B cell subgroups and initiated B cell transformation into malignant plasma cells by enhancing B cell proliferation and promoting plasma cell differentiation *in vitro* and *in vivo*. FCRL5 facilitated B cell differentiation into malignant plasma cells through its interaction with the IRF4/SPI1 complex. The use of targeted FCRL5 CAR T cells in patients with relapsed or refractory MM (RRMM) showed promising safety and efficacy. Together, our work identified genetic events linked to the initiation and malignant transformation of MM along the B cell lineage. These findings form the foundation for identifying potential therapeutic strategies for patients with RRMM by targeting MICs and their driving oncogenes.

INTRODUCTION

Multiple myeloma (MM) is a malignant hematologic tumor commonly found in middle-aged and elderly individuals, ranking as the second most prevalent hematologic malignancy (1). Over the past two decades, the introduction of new drugs such as proteasome inhibitors and immunomodulators (2), along with the widespread use of autologous hematopoietic stem cell (HSC) transplantation and chimeric antigen receptor T cell (CAR T cell) immunotherapy (3, 4), has enabled most patients with MM to achieve remission, with a median overall survival of 5 to 7 years (5). However, MM remains an incurable malignancy, with most patients experiencing relapse and progression, ultimately leading to refractory death (5, 6). Our studies have shed light on the role of dysregulated chromosome instability-

related genes (7, 8) and abnormal amino acid metabolism (9–11) in the bone marrow (BM) microenvironment in inducing drug resistance. Despite extensive research on MM progression, the mechanisms driving its initiation require further investigation.

MM is considered a disease of malignant plasma cells (PCs) that originate from PCs in the BM. Anti-PC therapy has not yet achieved a cure for MM, which may be due to the malignant transformation in MM-initiating cells (MICs) and their driving genes. New approaches focusing on the origins of MM malignant cells at the cellular and molecular levels are necessary to understand the stages and characteristics of these cells.

Tumor development is a multigene and multistep process (12). Normal cells undergo genetic hits, leading to the initiation of tumors (13). The pathogenesis of MM involves several genetic alterations including primary cytogenetic abnormalities in PCs, such as several translocations involving chromosome 14q, gain of chromosome 1q (1q^{Amp}, mainly amplified in the 1q21.1–1q32.2 region), and loss of chromosome 17p (17p^{Del}, mainly in the 17p13 region, for example, TP53) (14). It is proposed that most MICs originate from B cells (BCs) in the germinal center on the basis of the surface immunophenotypes, CD138⁻CD19⁺CD20⁺CD27⁺ memory BCs (15, 16), and a small fraction from BM, according to recent estimates based on MM cells, c-kit⁺ HSCs (17), and CD138⁺ PCs (18).

PC development proceeds from HSCs, multilymphoid progenitors (MLPs), pre-BCs, mature BCs, and plasmablasts (PBs) and ultimately to mature PCs (19). PCs, as terminally differentiated cells with low self-renewal and proliferative capabilities, are slow to proliferate *in vitro* and form tumors *in vivo*. Hence, understanding MICs requires tracing back to earlier lineages of PCs. The development of single-cell technology has facilitated MIC screening and identification, with recent cellular-resolution studies identifying progenitor

¹State Key Laboratory of Experimental Hematology, Key Laboratory for Carcinogenesis and Invasion, Chinese Ministry of Education, Key Laboratory of Carcinogenesis, Chinese Ministry of Health, National Clinical Research Center for Geriatric Disorders, FuRong Laboratory, Department of Hematology, Xiangya Hospital, Central South University, Changsha 410008, China. ²Cancer Research Institute, School of Basic Medical Sciences, Central South University, Changsha 410078, Hunan, China. ³Academy of Military Medical Sciences, Beijing 100850, China. ⁴Blood Diseases Institute, Xuzhou Medical University, Xuzhou 221002, China. ⁵Institute of Hematology & Blood Diseases Hospital, Chinese Academy of Medical Science & Peking Union Medical College, Tianjin 300074, China. ⁶Shanghai-MOST Key Laboratory of Health and Disease Genomics, Shanghai Institute for Biomedical and Pharmaceutical Technologies, Shanghai 200237, China. ⁷State Key Laboratory of Common Mechanism Research for Major Diseases, Institute of Basic Medical Sciences, Chinese Academy of Medical Sciences/Peking Union Medical College, Beijing 100005, P.R. China. ⁸Peking Union Medical College Hospital, Chinese Academy Medical Society & Peking Union Medical College, Beijing 100730, China. ⁹Xiangya School of Public Health, Central South University, Changsha 410013, Hunan, China. ¹⁰Department of Pharmacology and Pharmacy, University of Hong Kong, Hong Kong 999077, China.

*Corresponding author. Email: wenzhou@csu.edu.cn (W.Z.); chenhb@bmi.ac.cn (H.C.); chengtao@ihcams.ac.cn (T.C.); lihmd@163.com (K.X.)

†These authors contributed equally to this work.

subpopulations in various tumors (20, 21). In this study, we aimed to capture key genetic events associated with MM initiation along the hematopoietic stem cell lymphoid lineage differentiation, especially in the BC lineage, providing the basis for the identification of potential therapeutic targets.

RESULTS

scRNA-seq reveals aberrant HSC-BC-PC differentiation in patients with MM

To explore the potential relationship between MICs and the HSC-to-PC differentiation pathway, we used single-cell RNA sequencing (scRNA-seq) to investigate abnormalities in this pathway and identify potential MIC subpopulations in patients with MM (Fig. 1A). We sorted lin⁻CD34⁺CD38⁻ HSCs, CD19⁺ BCs, and CD38⁺CD138⁺ PCs from one healthy donor (HD) and two patients with new diagnosis MM (NDMM) (fig. S1A) for 10x Genomics scRNA-seq. After stringent quality control, we screened 17,465 cells and refined the annotation of these cells on the basis of public data (22, 23), which were consistent in the expression of corresponding marker genes (Fig. 1B; fig. S1, B to D; and table S1).

On the basis of the prediction of HSC differentiation potential reported in the literature (22), we observed that *AVP* and *CRHBP* were highly expressed in HSC and multipotent progenitor populations (MPPs). *CD79A* and *DNTT* were specifically expressed in MLPs, *CA1* and *PBX1* were activated in megakaryocyte-erythrocyte progenitors (MEPs), and *MPO* was coexpressed with *ELANE* in granulocyte-macrophage progenitors (GMPs), demonstrating consistency with previous observations (fig. S1, E to G). Compared with HDs, the proportion of HSCs in patients with MM decreased, whereas the proportion of lymphoid multipotent progenitors increased, suggesting that HSCs were suppressed and lymphoid differentiation increased in patients with MM (Fig. 1C).

Next, we divided BCs into early and mature BCs on the basis of their expression of *IL7R* and *CD10* (early) and *CD20* and *CD27* (mature). We further refined the early BCs into two subsets (pro B and pre B) and the mature BCs into naïve (naïve B) and memory-like BC (Mem B) subsets on the basis of previous reports (fig. S1F) (24, 25). Compared with HDs, the proportion of mature BCs in patients with MM increased, and the proportion of early BCs decreased (Fig. 1D), suggesting that BC differentiation was more mature in patients with MM. Furthermore, when our dataset was integrated with published data (26–28), the findings were consistent with above-mentioned results (fig. S2, A to E). Further flow cytometric analysis of cell subsets in HDs and patients with MM showed that the proportions of HSCs, MEPs, and total BCs were decreased, but the proportions of MLPs and PCs increased in patients with MM versus HDs (Fig. 1E and fig. S2, F and G). Normal hemopoiesis was reduced to a greater extent when there was greater PC infiltration of the BM (fig. S2H).

According to velocity analysis, which captures cellular dynamics involved in cell differentiation (29, 30), HDs have a clear differentiation pathway of HSCs to BCs to PCs. However, in patients with MM, we observed a bias on the differentiation trajectories of HSCs and BCs (Fig. 1F), and BCs in patients with MM had a lower developmental potency score (fig. S3A). To further clarify the changes in BC subsets in patients with MM, we selected HDs and NDMM for Smart-seq2 on the basis of the currently defined markers for pro B, pre B, immature B, naïve B, B regulatory (B_{reg}), memory BCs, and PCs (fig. S3,

B to G). The bias on differentiation trajectories was also observed in these patients (Fig. 1G), and correlation analysis between individual cell populations showed a positive correlation between immature BCs and memory BCs (Fig. 1H). These results implied that the changes in cell proportion in patients with MM may be caused by abnormal cell differentiation in the BM.

We further selected CD19⁺ BCs from HDs and patients with MM for in vitro culture, finding that BCs from patients with MM were more likely to differentiate into CD138⁺ PCs in vitro (fig. S3H). These results suggested that HSC and myeloid differentiation was inhibited in patients with MM, whereas lymphoid differentiation increased and BC differentiation became more mature (Fig. 1I). The differentiation of HSCs in patients with MM was abnormal, but further investigation was needed to determine the cell subsets or genetic abnormalities involved in this process.

BC subgroups exhibit 1q^{Amp} and t(4;14) but not 17p^{Del}

The same genetic event occurring in distinct cells within a tissue leads to different tumor phenotypes. Cells that acquire the first genetic hit are referred to as tumor-initiating cells and play a crucial role in the development of cancer (13). Thus, investigating MM onset requires the understanding of the origin of normal PCs and the primary genetic events in these cells. To further study the origin of MM cells, we used genetic tracing methods of copy number variation (CNV) analysis based on scRNA-seq and fluorescence in situ hybridization (FISH) to determine whether the abnormal changes in HSCs, BCs, and PCs were due to genetic events.

First, we used CNV analysis to investigate the abnormal chromosomal changes in HSCs, BCs, and PCs from two patients with MM. The first patient (MM1) exhibited both 17p^{Del} and 1q^{Amp}, whereas the second patient (MM2) had only 1q^{Amp}. The genetic alterations 1q^{Amp} and 17p^{Del} were estimated to originate from PCs and closely related to poor prognosis in MM. The CNV analysis showed 1q^{Amp} in PCs from both patients and 17p^{Del} in PCs from MM1 (Fig. 2A). The proportion of 1q^{Amp} was comparable to clinical detection results (fig. S4A), confirming the accuracy of CNV detection. Then, we detected 1q^{Amp} in BCs but not in HSCs (Fig. 2A). To obtain a higher resolution of subchromosomal CNVs, we calculated the averaged CNV score for each cell type on chromosomes 1 and 17. The results showed 17p^{Del} only in PCs of MM1 but not in BCs and HSCs. 1q^{Amp} was also detected in both patients in PCs and BCs but not HSCs (Fig. 2B).

To investigate other genetic alterations in BCs or HSCs that occur before PC differentiation, we used a public scRNA-seq database from patients with genetic abnormalities (28). We focused on two MM-related genetic alterations in PCs, t(4;14)(FGFR3/IgH) and t(11;14)(CCND1/IgH), and assessed *FGFR3* and *CCND1* expression. Both were highly expressed in PCs from patients with MM, indicating that scRNA-seq data can reflect genetic events by gene expression (fig. S4B). Because of the limited number of cells with these alterations in BCs and progenitors, we analyzed scRNA-seq gene expression profiles. *FGFR3* was expressed in a small subset of BCs and stem/progenitor cells from t(4;14) patients, but *CCND1* was detected in both t(11;14) and non-t(11;14) patients (fig. S4C). Single-cell polymerase chain reaction array results also showed that *FGFR3* was highly expressed in BCs from patients with MM, with increasing differences during PC differentiation, and was coexpressed with *MUC1* (mucin 1) in CD34⁺CD138⁺ cells (fig. S4, D to F). Next, we sorted HSCs-PCs using FISH with 1q21/TP53 probes for 1q^{Amp} and

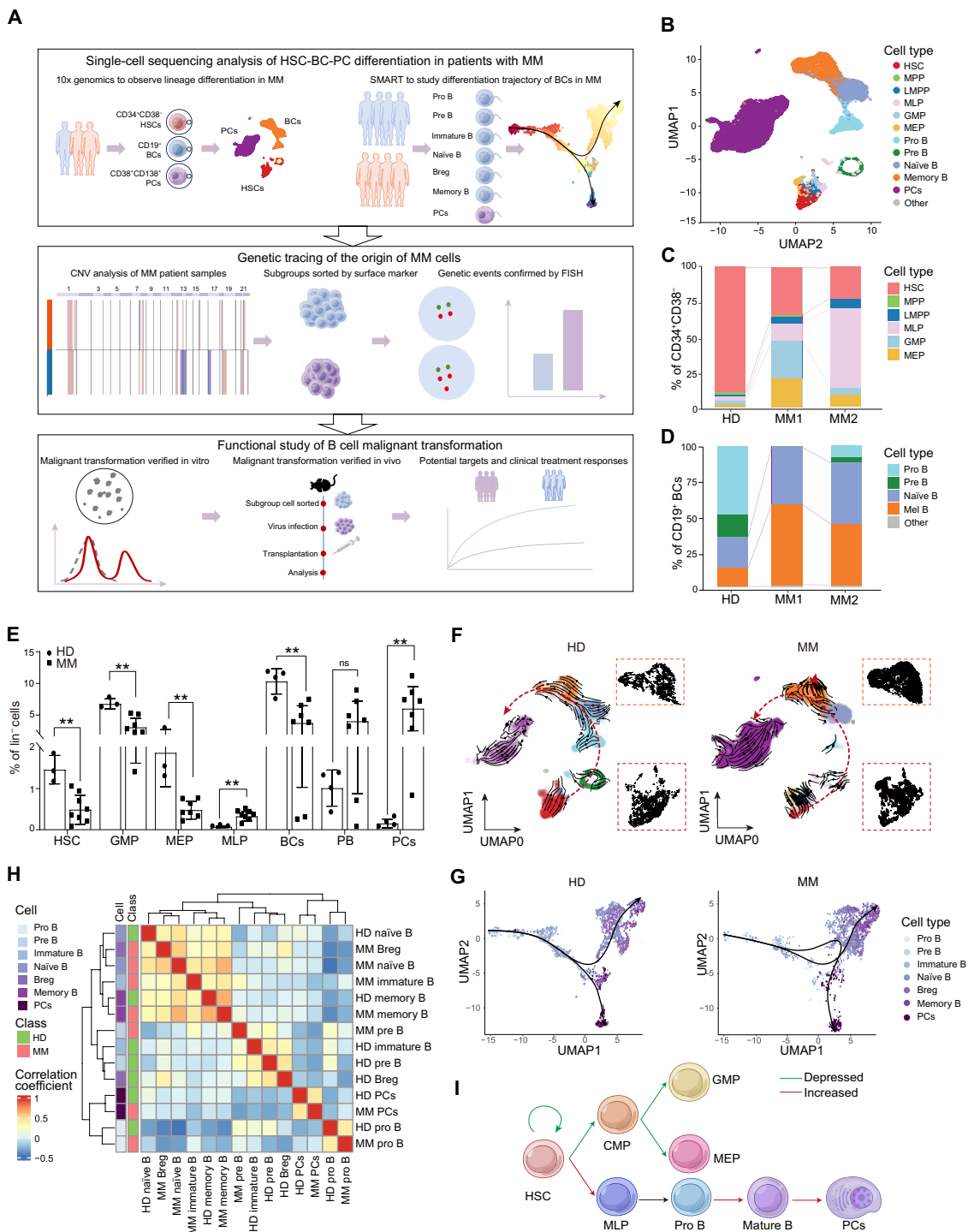


Fig. 1. Aberrant HSC lymphoid lineage differentiation in patients with MM. (A) Experimental approach for identifying and validating the origins of MM along HSC lymphoid lineage differentiation. (B) UMAP plot of pooled HSCs, BCs, and PCs identified in BM from HDs and two patients with MM from scRNA-seq data, colored by cell type. (C) Bar plot showing the ratio of each cluster among total HSCs; data from scRNA-seq data of one HD and two patients with MM. (D) Bar plot showing the ratio of each cluster among total BCs; data from scRNA-seq data of one HD and two patients with MM. (E) Flow cytometry analysis of the percentage of six cell populations, HSCs, MLPs, BCs, PBs, PCs, and MEPs, in the BM of HDs ($n = 4$) and patients with MM ($n = 7$). Data are presented as the means \pm SD; two-way ANOVA and Šidák's test; ** $P < 0.01$. ns, not significant. (F) RNA velocity analysis showing the differentiation from HSCs-BCs-PCs projected onto UMAP plot B. The solid black arrows represent RNA velocity flow projected in the UMAP space, and the dashed red arrows are manually marked according to known differentiation directions. Data from scRNA-seq data of one HD and two patients with MM. (G) UMAP plots showing BCs and PCs of Smart-seq2 scRNA-seq data. Each dot for a single cell, colored by cell type sorted by fluorescence-activated cell sorting. The dashed arrows are manually marked according to known differentiation directions. (H) Spearman correlation of the cells from Smart-seq2 scRNA-seq data. (I) Schematic outlining aberrant lymphoid lineage differentiation in HSCs from patients with MM.

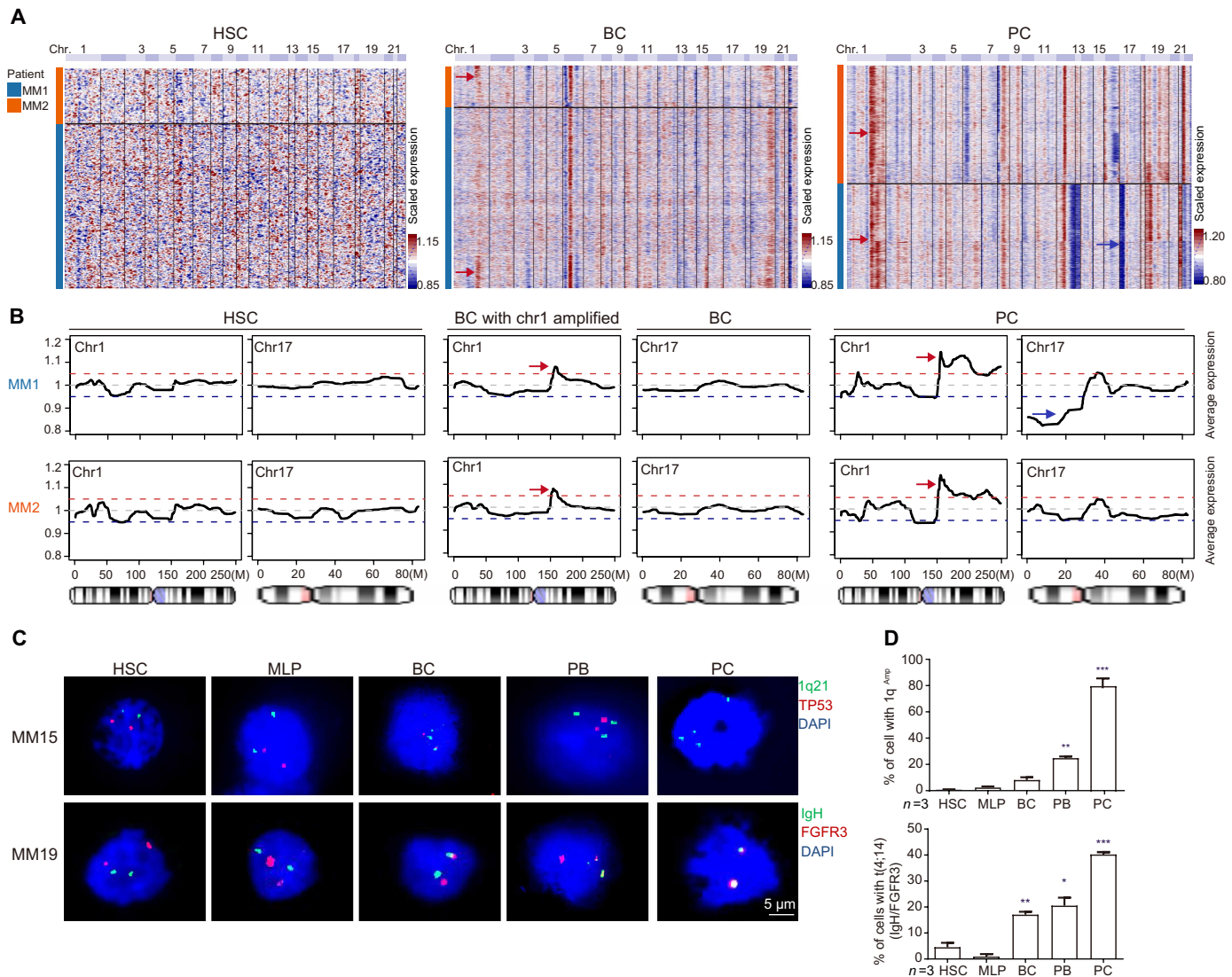


Fig. 2. scRNA-seq reveals genetic events originating from HSC differentiation hierarchy. (A) Heatmaps of CNV signals obtained from HSC differentiation (HSCs-BCs-PCs) by inferCNV. scRNA-seq data of two patients with MM were normalized against those of one HD, with genes ordered from left to right across the chromosomes (Chr). (B) Averaged CNV signals on Chr1 and Chr17, with genes ordered from left to right across the position on each chromosome. Red and blue dashed lines represent the values when the CNV signals are 1.05 and 0.95, respectively. (C) 1q21(green) and TP53(red) probe for 1q^{Amp} and 17p^{Del} (top) and FGFR3/IgH probe for t(4;14) (bottom) detected from HSC differentiation by FISH. Scale bar, 5 μm. (D) Proportion of 1q^{Amp}/TP53^{Del} (top) and FGFR3/IgH translocation (bottom) calculated from 100 cells from each patient with MM from (C). Data are presented as the means ± SD; n = 3; one-way ANOVA and Tukey's test; *P < 0.05, **P < 0.01, and ***P < 0.001.

17p^{Del} patients and IgH/FGFR3 probes for t(4;14) patients. 1q^{Amp} and IgH/FGFR3 fusion signals were in BCs, but TP53^{Del} was only in PCs (Fig. 2, C and D). These results suggested that different genetic variations in MM may originate from different stages of PC differentiation.

1q^{Amp} appears to originate from the CD24⁻FCRL5⁺ BC subpopulation

To further clarify the molecular characteristics of BC subsets with 1q^{Amp}, we divided BCs into six subsets on the basis of key genes for BC maturation: pro B, pre B, naïve B, Mel 1, Mel 2, and Mel 3 (Fig. 3A and fig. S5, A and B). We found that 83% of 1q^{Amp} cells were located in the Mel 2 subset (Fig. 3, B and C). We further checked the distribution of these cells in uniform manifold approximation

and projection (UMAP) of HSCs-PCs and found that BCs differentiated toward MM cells were more likely to be located in the Mel 2 subset (fig. S5C), suggesting that this subset is closely related to the development of MM.

To further screen the surface marker molecules of this subset for functional studies, we first analyzed and screened the top five unique markers of each BC subset (Fig. 3D), finding that *CIB1*, *FCRL5*, *MS4A1*, *NEAT1*, and *CRIP1* were highly expressed in the Mel 2 subset. Further analysis of surface markers and differentiation-related genes in BCs and PCs revealed particularly high expression of *CD20* and antibody secretion-related genes and low expression of the surface marker *CD24* in the Mel 2 subset (Fig. 3, E and F). Therefore, CD24⁻FCRL5⁺ could be used as a marker for this subset.

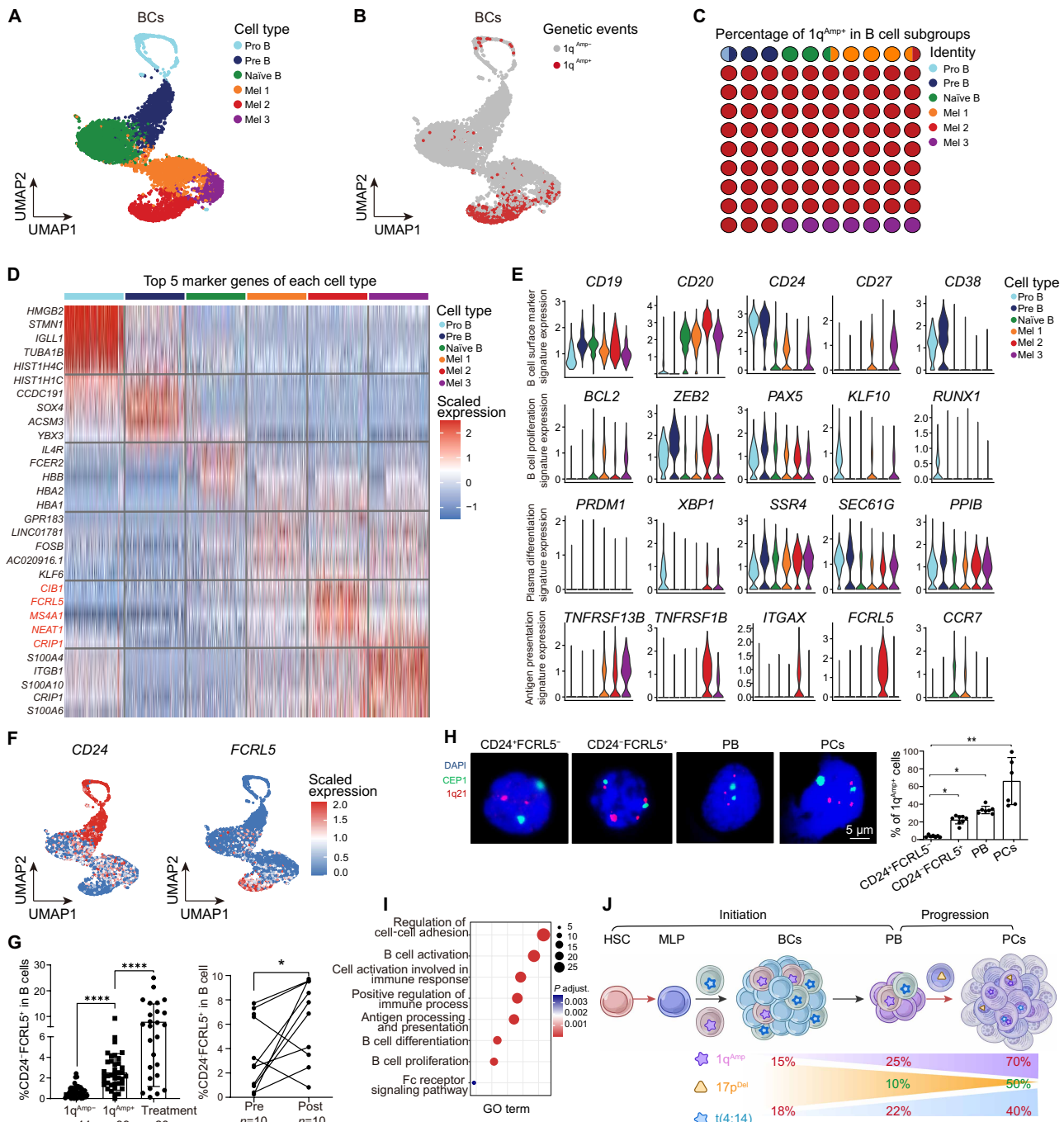


Fig. 3. 1q^{Amp} detected in CD19⁺CD24⁻FCRL5⁺ BC subgroups. (A to C) UMAP plot showing BCs from MM1, MM2, and HD1 of scRNA-seq, colored by (A) cell type or (B) whether the cell has chr1 amplification inferred by inferCNV. (A) UMAP plot showing six clusters of identified BC subgroups. (B) UMAP plot showing 1q^{Amp} cells in BC subgroups. (C) Dot plot showing the cell type proportion of 1q^{Amp} BCs. The 100 dots represent 639 1q^{Amp} BCs, and the colors represent the proportion of cell types. (D) Heatmap showing the scaled expression of the top five marker genes of each cell type. The genes were ordered by the average fold change, and each cell type was downsampled to 200 cells for visualization. The scale bar represents the scaled gene expression of each cell, processed via the scaling approach from Seurat. (E) Violin plots showing the expression of selected genes in each cell type. (F) UMAP plot of BCs colored by normalized expression of CD24 (left) and FCRL5 (right). Violin plots depict the probability density of the data at different expression levels, with the width of the shape representing the proportion of cells. (G) Flow cytometry analysis showing the proportion of CD24⁻FCRL5⁺ BCs derived from CD19⁺ cells in 1q^{Amp-} and 1q^{Amp+} at the diagnosis and treatment of patients with MM. Data are presented as the means \pm SD; 1q^{Amp-} (n = 44), 1q^{Amp+} (n = 39), and treatment (n = 26), one-way ANOVA and paired t test; patients with MM paired for treatment (n = 10), paired t test; *P < 0.05 and ***P < 0.0001. (H) 1q21(red) and CEP1(chromosome enumeration probe 1; control FISH probe detecting chromosome 1, green) probes for 1q^{Amp} detected from CD24⁻FCRL5⁻ BCs, CD24⁻FCRL5⁺ BCs, PBs, and PCs by FISH (left). Proportion of 1q^{Amp} cells derived from 100 cells from each patient with 1q^{Amp} MM (right). DAPI, 4',6-diamidino-2-phenylindole. Scale bar, 5 μm. Data are presented as the means \pm SD; n = 7; one-way ANOVA and Tukey's test; *P < 0.05 and **P < 0.01. (I) GO analysis of up-regulated genes (198 genes, adjusted P value < 0.05 and averaged log₂ fold change > 0.5) for 1q^{Amp} BCs versus other BCs. (J) Cloning evolution schematic of 1q^{Amp} from BCs-PCs based on CNV analysis and FISH.

We next detected the proportion of the CD24⁻FCRL5⁺ subset in patients with 1q^{Amp-} and 1q^{Amp+} MM. The proportion was significantly ($P = 0.036$) higher in 1q^{Amp+} (3%) than in 1q^{Amp-} (0.5%) patients. In addition, the proportion of the CD24⁻FCRL5⁺ subset increased in conventionally treated patients with MM (Fig. 3G). According to receiver operating characteristic analysis, the proportion of CD24⁻FCRL5⁺ BC subsets can distinguish MM with 1q^{Amp} (fig. S5D). Using a cutoff of 1%, an elevated proportion of CD24⁻FCRL5⁺ BCs was significantly associated with the PC proportion ($P = 0.0126$), clinical stage ($p = 0.0187$), and 1q^{Amp} in patients with MM ($P < 0.0001$) (Table 1). These findings suggested that the proportion of CD24⁻FCRL5⁺ BCs is closely linked to MM progression. Next, we sorted CD24⁺FCRL5⁻ and CD24⁻FCRL5⁺ BC subsets, PBs, and PCs and performed FISH to detect 1q21 copy number changes. About 24% of CD24⁻FCRL5⁺ BC subsets had 1q^{Amp}, and this proportion increased along the PC differentiation axis (Fig. 3H).

To explore CD24 and FCRL5 effects on cell differentiation, we leveraged Dynamo (29)—an algorithm that constructs transcriptomic

vector fields of single cells and therefore enables in silico perturbation analyses, predicting both gene expression responses in individual cells and cell-fate diversions after genetic perturbations. The results showed that in BCs of HDs, in silico suppression of CD24 or overexpression (OE) of FCRL5 disrupted differentiation pathways (fig. S5, E and F). Similarly, in MM, simulating CD24 OE or FCRL5 suppression reversed the aberrant differentiation pathway of the Mel 2 subset (fig. S5, E and F). To clarify the function of the 1q^{Amp+} BC subset, gene ontology (GO) term analysis was performed. GO analysis showed that marker genes of the CD24⁻FCRL5⁺ subset were enriched in BC proliferation, differentiation, and antibody secretion pathways (Fig. 3I). Together, these results suggested that the CD24⁻FCRL5⁺ BC subset may be the MIC subset of 1q^{Amp+} MM (Fig. 3J).

CD24⁻FCRL5⁺ BCs initiate malignant transformation by promoting BC proliferation and PC differentiation

To clarify the function of 1q^{Amp+} BC subsets, we explored the role of the CD24⁻FCRL5⁺ BC subset in BC proliferation and PC differentiation (Fig. 4A). First, using sequential transplantation for

Table 1. Correlation between the percentage of CD24⁻FCRL5⁺ in BCs and clinical characteristics in MM. ns, not significant; F, female; M, male; NA, not available; Plt, platelets; Hb, hemoglobin; ISS, International Staging System; DS, Durie-Salmon staging system.

Patients' characteristics	Low CD24 ⁻ FCRL5 ⁺ (<1% in BCs; n = 42)	High CD24 ⁻ FCRL5 ⁺ (>1% in BCs; n = 40)	P value
Gender (M/F/NA)	23/18/0	24/16/0	ns
Age (years)	61.5 ± 11.7	60.3 ± 10.4	ns
Plasma cells (%)	29	23	0.0126 [†]
Plt ($\times 10^9$)	197.6	181.9	ns
Hb (g/l)	88.8	95.4	ns
Bone destruction	20/42(47.7)	15/40(37.5)	ns
Subtype of MM			ns
IgG	16/42 (38.1)	17/40 (42.5)	
IgA	10/42 (23.8)	10/40 (25.0)	
κ/λ	6/42 (14.3)	5/40 (12.5)	
Nonsecretory	10/42 (23.8)	8/40 (20.0)	
ISS stage			0.0187 [*]
I	2/19 (10.5)	1/21 (4.8)	
II	7/19 (36.8)	5/21 (23.8)	
III	10/19 (52.6)	15/21 (71.4)	
DS stage			<0.0001 [*]
I	2/17 (11.8)	0/20 (0)	
II	1/17 (5.9)	0/20 (0)	
III	14/17 (82.3)	20/20 (100)	
Genetic events			
1q21 ^{Amp}	7/35(20.0)	32/38(84.2)	<0.0001 [*]
17p ^{Del}	1/32	2/34	ns
RB ^{Del}	10/32	10/34	ns
IgH translocation	3/13	10/14	<0.0001 [*]
t(4;14)	1/13	3/14	0.009 [*]

*P values calculated by using Fisher's exact test.

[†]P value calculated by using the two-tailed Welch's t test.

sphere-formation assay (31) in BCs from patients with MM, we found that $1q^{Amp+}$ MM BCs had a stronger continuous clonal expansion ability than $1q^{Amp-}$ MM (Fig. 4B, fig. S6A, and table S2). The proportion of FCRL5 $^+$ cells increased with continuous clonal expansion (fig. S6, B and C), suggesting that the sustained capacity of BCs for clonal expansion may be related to the relative abundance of FCRL5 $^+$ cells.

We sorted FCRL5 $^+$ and FCRL5 $^-$ cells from the sequential transplantation for sphere formation and found an increase in the number of FCRL5 $^+$ cell clones (Fig. 4C). Cellular morphology and flow cytometry analysis of CD138 expression (Fig. 4D and fig. S6D) showed that the FCRL5 $^+$ cell subset differentiated into more mature PCs. Further FISH testing showed that FCRL5 $^+$ cells had $1q^{Amp}$ (Fig. 4E) and a high expression of PC differentiation-related transcription factors (TFs) (fig. S6E).

Subsequently, we isolated FCRL5 $^+$ and FCRL5 $^-$ cells from the third clonal expansion BCs for subcutaneous implantation into B-NDG mice to assess their tumorigenic potential. The results demonstrated that both the tumor volumes and weights in the FCRL5 $^+$ group were greater than those observed in the FCRL5 $^-$ group ($P = 0.042$) (Fig. 4F) and showed an increased expression of CD138 and Ki67 (Fig. 4G), supporting the notion that the FCRL5 $^+$ subset may initiate malignant transformation.

To substantiate the hypothesis that malignant PCs in $1q^{Amp}$ MM originated from the CD24 $^+$ FCRL5 $^+$ subset, we sorted CD24 $^+$ FCRL5 $^-$ and CD24 $^+$ FCRL5 $^+$ BCs and PCs from the BM of patients with $1q^{Amp}$ MM for B cell receptor (BCR) sequencing (BCR-seq). Our analysis revealed a progressive decline in BCR diversity among CD24 $^+$ FCRL5 $^-$ and CD24 $^+$ FCRL5 $^+$ BCs and PCs (Fig. 4H). There was also an association between CD24 $^+$ FCRL5 $^+$ BCs and PCs in clone type (fig. S6F and table S3). Because BCR diversity is related to V gene mutations and combinations of the V region of the variable region of immunoglobulin heavy chains, we analyzed the proportions of V genes. Results indicated a single clonal type predominance among PCs (for example, IgHV3-48), with more than 50% representation of the same clone, consistent with MM as a monoclonal disease (Fig. 4I and fig. S6G). A predominant V gene of PCs was found in the CD24 $^+$ FCRL5 $^+$ subset but scarcely in the CD24 $^+$ FCRL5 $^-$ subset. Clonality models showed that the primary clone of malignant PCs comes from CD24 $^+$ FCRL5 $^+$ BCs (Fig. 4J), implying that this BC subset is the source of malignant PCs in MM.

Last, we analyzed the expression of genes associated with MM therapeutic targets, genes located in the chromosome 1q region, and TFs associated with PC differentiation in CD24 $^+$ FCRL5 $^-$ and CD24 $^+$ FCRL5 $^+$ BCs and PCs. The findings revealed an increased expression of genes from the 1q region and PC differentiation-related genes in CD24 $^+$ FCRL5 $^+$ BCs and PCs. However, MM CAR T cell therapy targets, such as B cell maturation antigen (BCMA) (32) and G protein-coupled receptor class C group 5 member D (GPRC5D) (33), were not expressed in the CD24 $^+$ FCRL5 $^+$ BC subset (Fig. 4K). Consequently, it is imperative to identify potential targets aimed at this subpopulation.

FCRL5 initiates BC transformation to plasma malignancy

FCRL5 is a surface molecule expressed on age-related BCs (34), which is associated with age and various immune-related diseases (35). This raised the question of whether the expansion of the CD24 $^+$ FCRL5 $^+$ BCs is linked to the malignant transformation of MM mainly affecting the elderly population.

To verify the relationship between the CD24 $^+$ FCRL5 $^+$ BCs, PC differentiation, and the occurrence of MM, we used BCs harvested from Cas9 $^{tg/+}$ mice to perform in vitro differentiation assays to investigate the requirement of FCRL5 for the differentiation of PCs. We assessed the number of differentiated cells and the proportion of induced PCs (iPCs) (Fig. 5A). Infection with FCRL5 OE viruses carrying green fluorescent protein (GFP) or Akaluc both increased PC differentiation, whereas single guide RNA (sgRNA) to knock down FCRL5 decreased it (Fig. 5, B to D, and fig. S7, A and B). Furthermore, the key factors of PC differentiation, *Blimp1*, *Xbp1*, and *Irif4*, were up-regulated in the FCRL5 OE group (Fig. 5, E and F), whereas sgRNA targeting FCRL5 decreased their expression (fig. S7C). In addition, adding FCRL5-neutralizing antibodies to the differentiation induction system produced similar results (fig. S7D), with the PC proportion gradually decreasing as the antibody concentration increased (fig. S7, E and F).

To further elucidate the role of FCRL5 in the malignant transformation of MM, we performed BC transfer experiments (36) using isolated IgM $^+$ BCs from the spleens of 40-week-old Vk^*Myc mice. The number of CD138 $^+$ PCs in the BM and spleen was quantified, and immunoglobulin G subclass 2b (IgG2b) concentrations were measured at week 18 (Fig. 5G). The FCRL5 OE group exhibited higher IgG2b concentrations (Fig. 5H), lymph node enlargement (fig. S7G), and PC enrichment (fig. S7H). GFP $^+$ (donor) cells in the BM showed a higher proportion of CD138 $^+$ (Fig. 5I); PC accumulation (Fig. 5J); and an increased expression of FCRL5, CD138, and Ki67 in tissue sections (Fig. 5K). Last, micro-computed tomography imaging indicated decreased bone density and increased bone destruction markers in the FCRL5 OE group (Fig. 5L). The t(4;14) (FGFR3/IgH) translocation was identified in BCs (Fig. 2, C and D). Therefore, we investigated the role of FGFR3 in BC differentiation and MM malignancy. Blocking FGFR3 expression inhibited PC differentiation in vitro (fig. S8, A to E), and FGFR3 OE accelerated MM progression in vivo (fig. S8, F to J). Collectively, these results underscored the critical role of FCRL5 and FGFR3 in PC differentiation and MM pathogenesis. However, the mechanism underlying how FCRL5 promotes BC malignant transformation remained unclear.

FCRL5 initiates BC transformation to plasma malignancy by interacting with the IRF4/SPI1 complex

To explore the regulatory mechanism of the malignant transformation of CD24 $^+$ FCRL5 $^+$ subgroups, we analyzed single-cell sequencing assay for transposase-accessible chromatin (scATAC-seq) data of paired scRNA-seq on BCs and assigned cell type information (Fig. 6A and fig. S9, A to C). Similarly, $1q^{Amp+}$ BCs were mainly in the Mel 2 subset (fig. S9D). Chromosome accessibility analysis showed an increase in open chromatin regions in $1q^{Amp+}$ BCs (Fig. 6B), and FCRL5 gene promoter chromatin regions had increased accessibility in the Mel 2 subset (fig. S9E). To identify potential TFs in $1q^{Amp+}$ cells, we used scRNA-seq and scATAC-seq with three strategies (Fig. 6C and table S4). First, we identified TFs with enriched motifs in more accessible chromatin regions of $1q^{Amp+}$ cells (fig. S9, F and G). Second, 27 TF motifs were scanned around the FCRL5 promoter (fig. S9H). Third, we identified the top 10 TFs with high regulatory activity scores in $1q^{Amp+}$ BCs (Fig. 6, D and E). On the basis of the above three strategies, SPI1 enrichment was found, with elevated SPI1 activity in the $1q^{Amp+}$ subset (Fig. 6C). Further analysis of chromatin immunoprecipitation sequencing (ChIP-seq) of GM12878 BCs showed that SPI1 and interferon regulatory factor 4 (IRF4) can bind

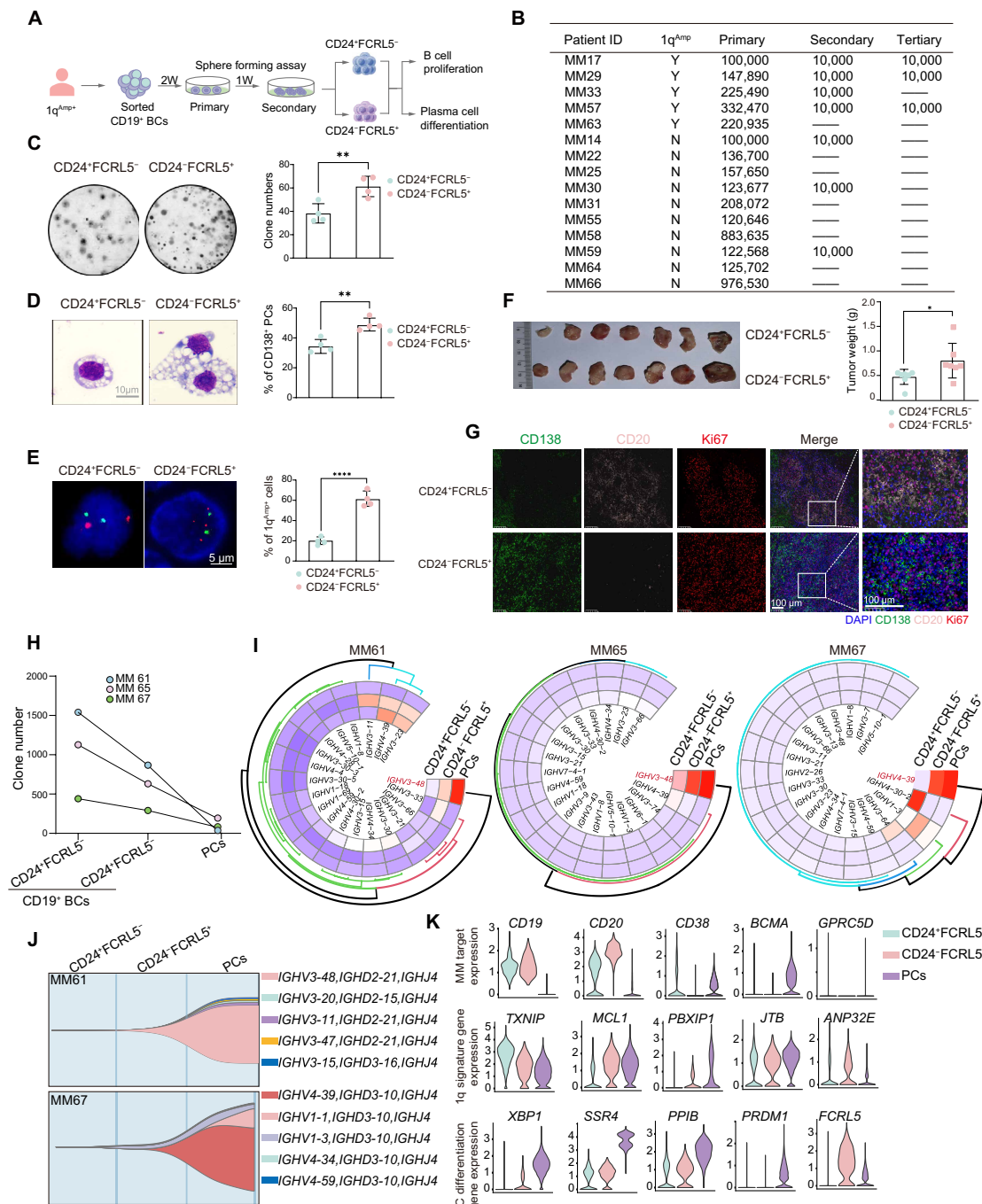


Fig. 4. CD19⁺CD24⁻FCRL5⁺ BCs are prone to differentiate to PCs. (A) Schematic diagram. An in vitro sequential spherulation culture of BCs from patients with MM was conducted to assess CD24⁺FCRL5⁺ BC subgroups. 2W, 2 weeks. (B) Cell counts of BCs in sequential spherulation cultures for each patient with MM. (C) Representative images of tertiary sphere-forming analysis in CD24⁺FCRL5⁻ and CD24⁺FCRL5⁺ BCs (images are shown in 1× magnification). Data are presented as the means \pm SD; $n = 4$; two-tailed Student's t test; ** $P < 0.01$. (D) Swiss-Giemsa staining of the cytomorphological changes of CD24⁺FCRL5⁻ and CD24⁺FCRL5⁺ BC subgroups by sphere-forming analysis. Scale bar, 10 μ m. Data are presented as the means \pm SD; $n = 4$; two-tailed Student's t test; ** $P < 0.01$. (E) Proportion of 1q^{Amp}⁺ cells among 100 cells of CD24⁺FCRL5⁻ and CD24⁺FCRL5⁺ BCs by FISH. Scale bar, 5 μ m. Data are presented as the means \pm SD; $n = 4$; two-tailed Student's t test; **** $P < 0.0001$. (F) Representative images of tumor xenografts in B-NDG mice after subcutaneous injection of BCs produced by sphere-forming assay in vitro. Tumor weights of xenografts derived from B-NDG mice injected with CD24⁺FCRL5⁻ and CD24⁺FCRL5⁺ BCs. Data are presented as the means \pm SD; $n = 7$; two-tailed Student's t test; * $P < 0.05$. (G) Representative images for immunohistochemistry detection of the tumor nodules derived from B-NDG mice injected subcutaneously with CD24⁺FCRL5⁻ and CD24⁺FCRL5⁺ BCs. Scale bar, 100 μ m. (H) Line chart showing the clone numbers of CD24⁺FCRL5⁻ and CD24⁺FCRL5⁺ BCs and PCs by BCR-seq. (I) Top 20 V gene usage frequency statistics of CD24⁺FCRL5⁻ and CD24⁺FCRL5⁺ BCs and PCs by BCR-seq. (J) FISH plot showing BCR-seq-based clonality models for CD24⁺FCRL5⁻ and CD24⁺FCRL5⁺ BCs and PCs. (K) Violin plots showing the expression of MM target genes, 1q signature genes, and PC differentiation genes in CD24⁺FCRL5⁻ and CD24⁺FCRL5⁺ BCs and PCs from scRNA-seq data. Violin plots depict the probability density of the data at different expression levels, with the width of the shape representing the proportion of cells.

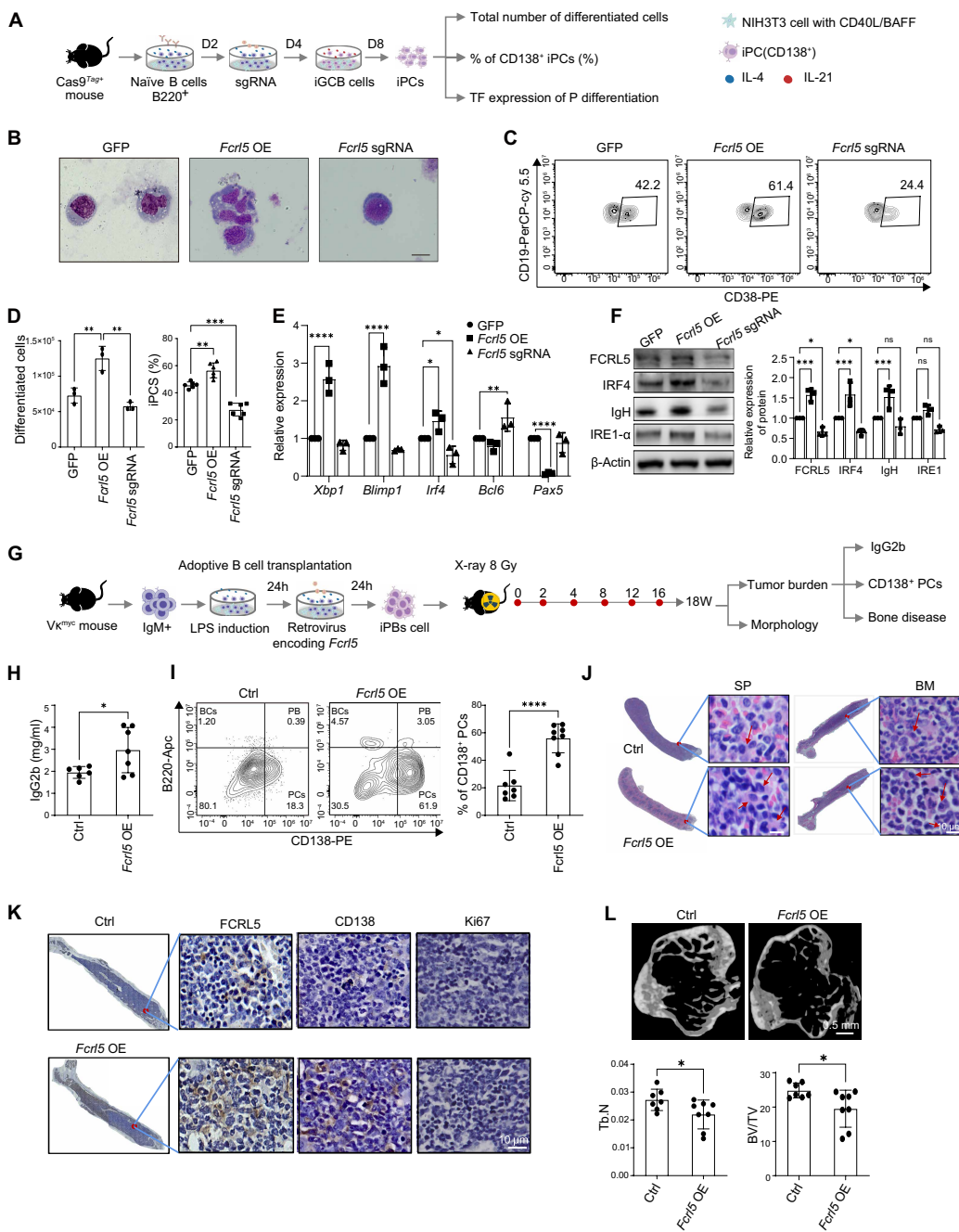


Fig. 5. FcRL5 promotes BC malignant transformation to MM cells. (A) Schematic of in vitro iPC differentiation from splenic naïve BCs. Naïve BCs were isolated from Cas9^{tg/+} mice. Cultured BCs were transduced with retroviruses encoding sgRNA of *Fcrl5* (*Fcrl5*-sgRNA) or *Fcrl5* OE vector (*Fcrl5* OE) at day 2. At day 8, iPCs among retrovirus-transduced Cas9-expressing BCs were analyzed by flow cytometry. iGCB cells, induced germinal center B cells; IL-4, interleukin-4; D2, day 2. (B) Wright-Giemsa staining of the iPC cytomorphological changes of control (Ctrl), *Fcrl5*-sgRNA, and *Fcrl5* OE groups. Scale bar, 10 μm; n = 7. (C) Flow cytometry analysis of iPCs among cultured Cas9^{tg/+} BCs transduced with retroviruses encoding Ctrl, *Fcrl5*-sgRNA, and *Fcrl5* OE. (D) Statistical analysis of the number of differentiated cells (left; n = 3) and proportion of iPCs (right; n = 6) shown in (C). Data are presented as the means ± SD; one-way ANOVA and Tukey's test; **P < 0.01 and ***P < 0.001. (E) Relative mRNA expression of BC and PCTFs in iPCs by reverse transcription polymerase chain reaction. Data are presented as the means ± SD; n = 3; two-way ANOVA and Šidák's test; *P < 0.05, **P < 0.01, and ****P < 0.0001. (F) Proteins of FCRL5, IgH chain, IRE1-α, IRF4, and actin were analyzed by immunoblotting. Data are presented as the means ± SD; n = 3, two-way ANOVA and Šidák's test; *P < 0.05 and ***P < 0.001. (G) Schematic diagram of the adoptive BC transplantation mouse model. LPS, lipopolysaccharide. (H) Serum concentrations of IgG2b in Ctrl (n = 6) and *Fcrl5*-OE (n = 7) adoptive BC transplantation mouse models by enzyme-linked immunosorbent assay. Data are presented as the means ± SD; two-tailed Student's t test; *P < 0.05. (I) Flow cytometry analysis of the proportion of CD138⁺ cells derived from Ctrl (n = 7) and *Fcrl5*-OE (n = 8) adoptive BC transplantation mice. Data are presented as the means ± SD; two-tailed Student's t test; ****P < 0.001. (J) Hematoxylin and eosin staining shows the morphology of PCs in the spleens (SP) and BM from Ctrl (n = 7) and *Fcrl5*-OE (n = 8) adoptive BC transplantation mice. Scale bar, 10 μm. (K) Representative images from immunohistochemistry detection of CD138 protein in adoptive BC transplantation mice. Ctrl (n = 7) and *Fcrl5*-OE (n = 8). Scale bar, 10 μm. (L) Micro-computed tomography images of femurs derived from adoptive BC transplantation mice. Tb.N, trabecular number; BV/TV, bone volume/total volume. Scale bar, 0.5 mm. Ctrl (n = 7) and *Fcrl5*-OE (n = 8). Data are presented as the means ± SD; two-tailed Student's t test; *P < 0.05.

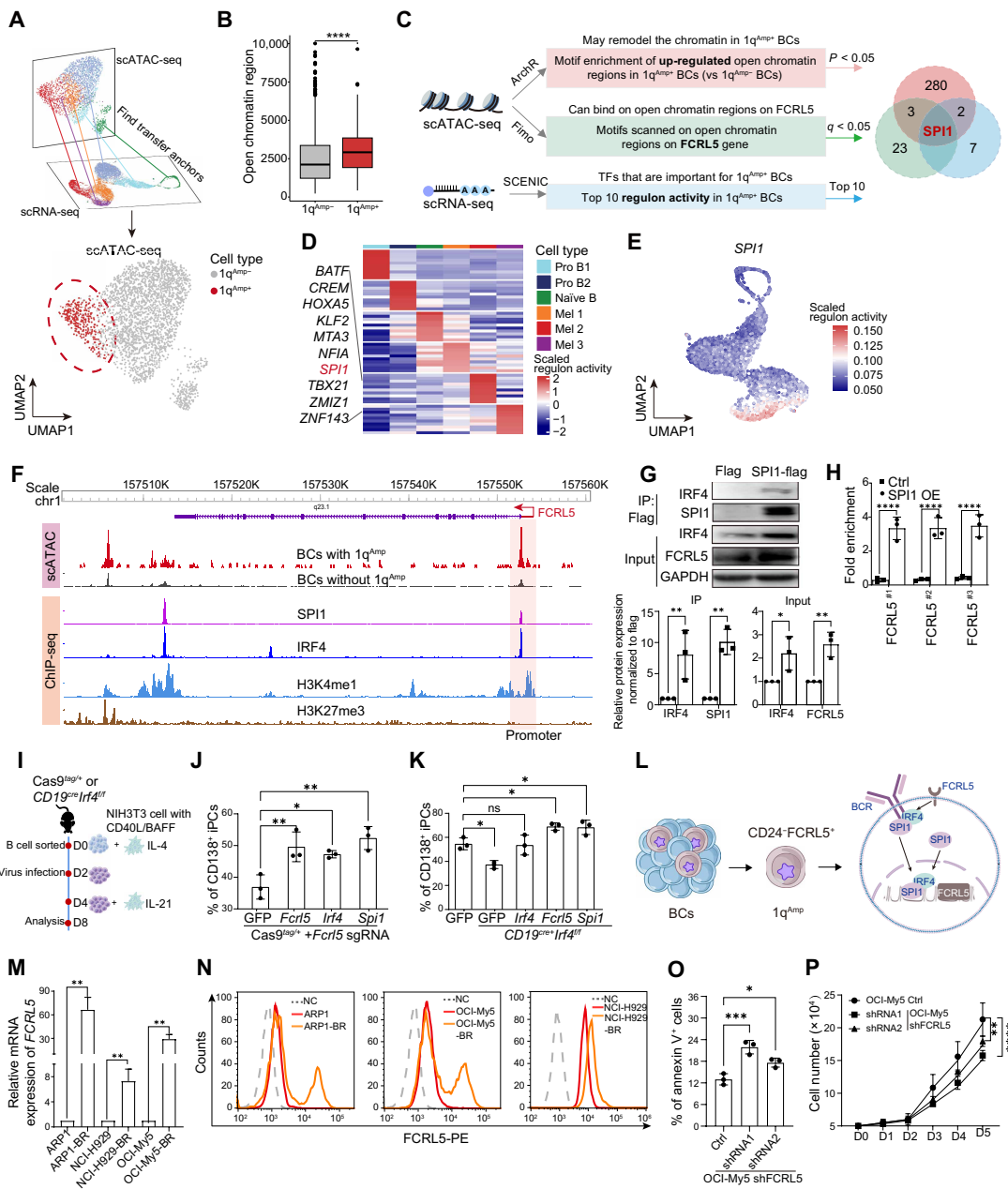


Fig. 6. FCRL5 induces PC differentiation by interacting with the IRF4/SPI1 complex. (A) Schematic diagram of mapping cell type label from scRNA-seq to scATAC-seq (left) and UMAP plot showing BCs from scATAC-seq, colored by whether the cell is 1q^{Amp+}. (B) Box plot showing the number of open chromatin regions of 1q^{Amp+}. scATAC-seq data for BCs originate from the same patient source as the scRNA-seq in Fig 3. Independent sample t test; **** $P < 0.0001$. (C) Workflow of identifying potential TFs that play important roles in 1q^{Amp+} cells. (D) Heatmap showing the top 10 regulon activity TFs in each cell type. The scale bar represents the scaled averaged regulon activity of each cell type, inferred by SCENIC using scRNA-seq. (E) UMAP plot of BCs colored by the regulon activity of SPI1. The scale bar represents the scaled activity of each cell type, inferred by SCENIC using scRNA-seq. (F) Genome tracks showing the averaged scATAC-seq profiles of 1q^{Amp+} and 1q^{Amp-} BCs (top) and ChIP-seq profiles of GM12878 cells from the WashU epigenome browser (bottom). (G) Exogenous SPI1 was pulled down by SPI1 antibodies in GM12878 cells with or without SPI1 OE, and the IRF4 proteins were analyzed by immunoblotting. The lysates before immunoprecipitation (IP) were used as a positive control. Data are presented as the means \pm SD; $n = 3$; two-way ANOVA and Šidák's test; * $P < 0.05$ and ** $P < 0.01$. (H) ChIP confirmed that the TF SPI1 specifically binds to the FCRL5 promoter region. Data are presented as the means \pm SD; $n = 3$; two-way ANOVA and Šidák's test; **** $P < 0.0001$. (I) Schematic of in vitro iPC differentiation from splenic naïve BCs. Naïve BCs were isolated from Cas9^{tg/+} mice and CD19^{tg/+}, Irf4^{tf}. (J) Flow cytometry analysis of iPCs among cultured Cas9^{tg/+} BCs transduced with retroviruses encoding GFP, FCRL5, SPI1, and IRF4 combined with FCRL5 sgRNA. Data are presented as the means \pm SD; $n = 3$; one-way ANOVA and Tukey's test; * $P < 0.05$ and ** $P < 0.01$. (K) Flow cytometry analysis of iPCs among cultured CD19^{tg/+}, Irf4^{tf} BCs transduced with retroviruses encoding GFP, FCRL5, SPI1, and IRF4. Data are presented as the means \pm SD; $n = 3$; one-way ANOVA and Tukey's test; * $P < 0.05$. (L) Schematic of the working model for how FCRL5 promotes BC malignant transformation by interacting with the IRF4/SPI1 complex. (M) Relative mRNA expression of FCRL5 in the three BR cell lines was detected with quantitative polymerase chain reaction. Data are presented as the means \pm SD; $n = 3$; two-tailed Student's t test; ** $P < 0.01$. (N) Relative protein expression of FCRL5 in the three BR cell lines was detected with flow cytometry. (O) Statistical analysis of the percentage of apoptotic cells after shFCRL5 treatment. Data are presented as the means \pm SD; $n = 3$; one-way ANOVA and Tukey's test; * $P < 0.05$ and *** $P < 0.001$. (P) Growth curves of OCI-My5 scramble and shFCRL5 cells cultured for 5 days. Data are presented as the means \pm SD; $n = 3$; one-way ANOVA and Tukey's test; ** $P < 0.01$ and **** $P < 0.0001$.

to the *FCRL5* promoter region (Fig. 6F), and an enhancer marker signal was detected, suggesting that SPI1/IRF4 binding may regulate *FCRL5* transcriptional activity.

IRF4 can interact with SPI1 as an important component of the BCR, regulating BC activation and PC differentiation (37, 38). Initially, we demonstrated the interaction between SPI1 and IRF4 proteins (Fig. 6G). Subsequently, we confirmed the binding of SPI1 to the promoter region of *FCRL5* (Fig. 6H). Furthermore, OE of IRF4 and SPI1 in *FCRL5*-knockdown cells could reverse the reduction in PC differentiation (Fig. 6, I and J, and fig. S9, I and J). In *CD19^{cre}IRF4^{fl/fl}* conditional knockout mice, OE of FCRL5 and SPI1 also reversed the decrease in PC differentiation (Fig. 6K and fig. S9, K to L). Furthermore, SPI1 was overexpressed in BCs, promoting PC differentiation (fig. S9, M and N). Together, these results indicated that *FCRL5* OE directly promoted BC proliferation and induced nuclear localization of SPI1 and up-regulation of IRF4, thus promoting PC differentiation (Fig. 6L). In addition, we further investigated the role of FCRL5 in MM. First, we assessed FCRL5 expression in six widely used MM cell lines and three bortezomib-resistant (BR) cell lines (Fig. 6, M and N, and fig. S10, A and B). The result showed that FCRL5 was highly expressed in all three BR cell lines, with increases observed in ARP1-BR and OCI-My5-BR cell lines. Knockout of FCRL5 promoted apoptosis (Fig. 6O and fig. S10, C and D) and inhibited cell proliferation (Fig. 6P). The OE of FCRL5 in the GM12878 cell line (fig. S10, E and F) enhanced BC proliferation (fig. S10G), elevated the expression of TFs Blimp1 (B lymphocyte–induced maturation protein 1) and IRF4, and increased the nuclear localization of SPI1 (fig. S10H). These results further supported the potential of FCRL5 as a therapeutic target in MM treatment.

Targeted FCRL5 CAR T cells achieve high safety and efficacy in patients with relapsed or refractory MM

To further explore the therapeutic relevance of FCRL5, we designed CAR vectors on the basis of the FCRL5 antigen-binding site (39), CD8 α stalks, and the 4-1BB domain (fig. S11A). The infection of T cells by the CAR virus demonstrated an efficiency exceeding 50% (fig. S11B) and reduced the proportion of CD138 $^{+}$ MM cells in the coculture system (fig. S11C). Furthermore, we intravenously inoculated luciferase-expressing OCI-My5 cells and BCs with FCRL5 OE (GM12878-FCRL5 OE) into B-NDG mice (Fig. 7A) and injected mice with double the amount of CAR T cells as the number of tumor cells they received. CAR T cells originated from three different donors and were injected on the 10th day. The results showed significantly ($P = 0.0052$) lower tumor luminescence in the CAR-FCRL5 group; however, there was no significant difference in the low FCRL5 expression group (GM12878-EV) (Fig. 7B and fig. S11, D to F).

We proceeded to conduct a phase 1 clinical trial to evaluate the safety and efficacy of FCRL5 CAR T cell therapy in treating patients with relapsed or refractory MM (RRMM) (ClinicalTrials.gov, NCT0196255) (Fig. 7C). Three patients were enrolled according to the expression of FCRL5 in BCs (Fig. 7D). In the final infusion products of CAR-FCRL5 T cell for patients, the average percentages of CAR integration were about 20 and 60%, respectively (table S5). The patients received a lymphodepleting chemotherapy regimen consisting of cyclophosphamide and fludarabine, followed by a single infusion of FCRL5 CAR T cells at doses ranging from 0.56×10^6 to 2.35×10^6 cells per kilogram of body weight and periodical check of the abundance of CAR T cells after infusion to evaluate the expansion of CAR T cells (Fig. 7E). Mild cytokine release syndrome

occurred in patients after infusion of FCRL5 CAR T cells, and immune effector cell–associated neurotoxicity syndrome was not observed (Fig. 7F). During a median observation period of 1 month, three patients achieved partial remission, as evidenced by the concentrations of free light chains in serum and urine [patient 1 and patient 2 with RRMM (RRMM1 and RRMM2); Fig. 7G] or B-scan ultrasonography [patient 3 (RRMM3); Fig. 7H]. Collectively, these data indicated that FCRL5 CAR T cells demonstrate safety and efficacy for patients with MM.

To enhance the clinical efficacy in MM treatment, we thought to integrate first-line clinical therapies with dual targeting of both tumor and initiating cells. This approach could potentially reduce the likelihood of recurrence in patients with MM. Consequently, we have developed dual-target CAR T cells that target both FCRL5 and BCMA. After assessing BCMA expression (fig. S11G), we intravenously inoculated luciferase-expressing MM.1s cells into B-NDG mice to obtain a humanized MM mouse model. We then injected twice as many CAR T cells as tumor cells on the seventh day (Fig. 7I). The results demonstrated a significant ($P < 0.0001$) reduction in tumor luminescence in the CAR-BCMA and CAR-FCRL5&BCMA groups compared with the CAR-FCRL5 group, although no significant difference was observed between the CAR-FCRL5 and CAR-BCMA groups (Fig. 7J). Survival analysis further indicated that CAR T cells targeting FCRL5 and BCMA effectively mitigated MM progression (Fig. 7K). The aforementioned results indicated that targeting FCRL5 is both safe and effective in patients with RRMM.

DISCUSSION

Tumors originate from normal cells that have undergone malignant transformation as a result of genetic alterations (13, 40). The initiation of MM is complex, involving unclear mechanisms of MICs, which cause incurable malignancy (6). This study used single-cell sequencing and genetic tracing across HSC-to-lymphoid lineage differentiation in patients with MM to identify abnormal differentiation activities. Specifically, we observed 1q^{Amp} in a CD24 $^{-}$ FCRL5 $^{+}$ BCs subgroup, with TP53 deletion observed in the PC stage, and found that 1q^{Amp} in this subgroup initiates malignant transformation to PC malignancy by promoting BC proliferation and PC differentiation in vitro and in vivo. We identified FCRL5 as initiating this process through interaction with the IRF4/SPI1 complex (fig. S12). Targeted FCRL5 CAR T cells in patients with RRMM achieved high safety and efficacy, providing new intervention strategies.

The cell of origin of cancer is the normal cell that receives the first genetic hit, whereas cancer stem cells are the cancer cells that maintain tumor propagation (31). The initiation and progression of MM are highly intricate processes, attributable not only to the differentiation of PCs from HSCs but also to the presence of numerous genetic alterations. Therefore, in studying the process of malignancy, we must consider both the common characteristics of tumor-initiating cells and the unique properties of differentiation of PCs. We used single-cell sequencing and genetic tracing across HSC-to-lymphoid lineage differentiation in patients with MM to identify abnormal differentiation activities. Specifically, we observed 1q^{Amp} in a CD24 $^{-}$ FCRL5 $^{+}$ BCs subgroup, with TP53 deletion observed in the PC stage to maintain the MM cell propagation.

Transcriptomics allowed us to identify biomarkers within subpopulations, and scATAC-seq uncovered regulatory mechanisms. Different detection methods, including integrated single-cell analysis, FISH,

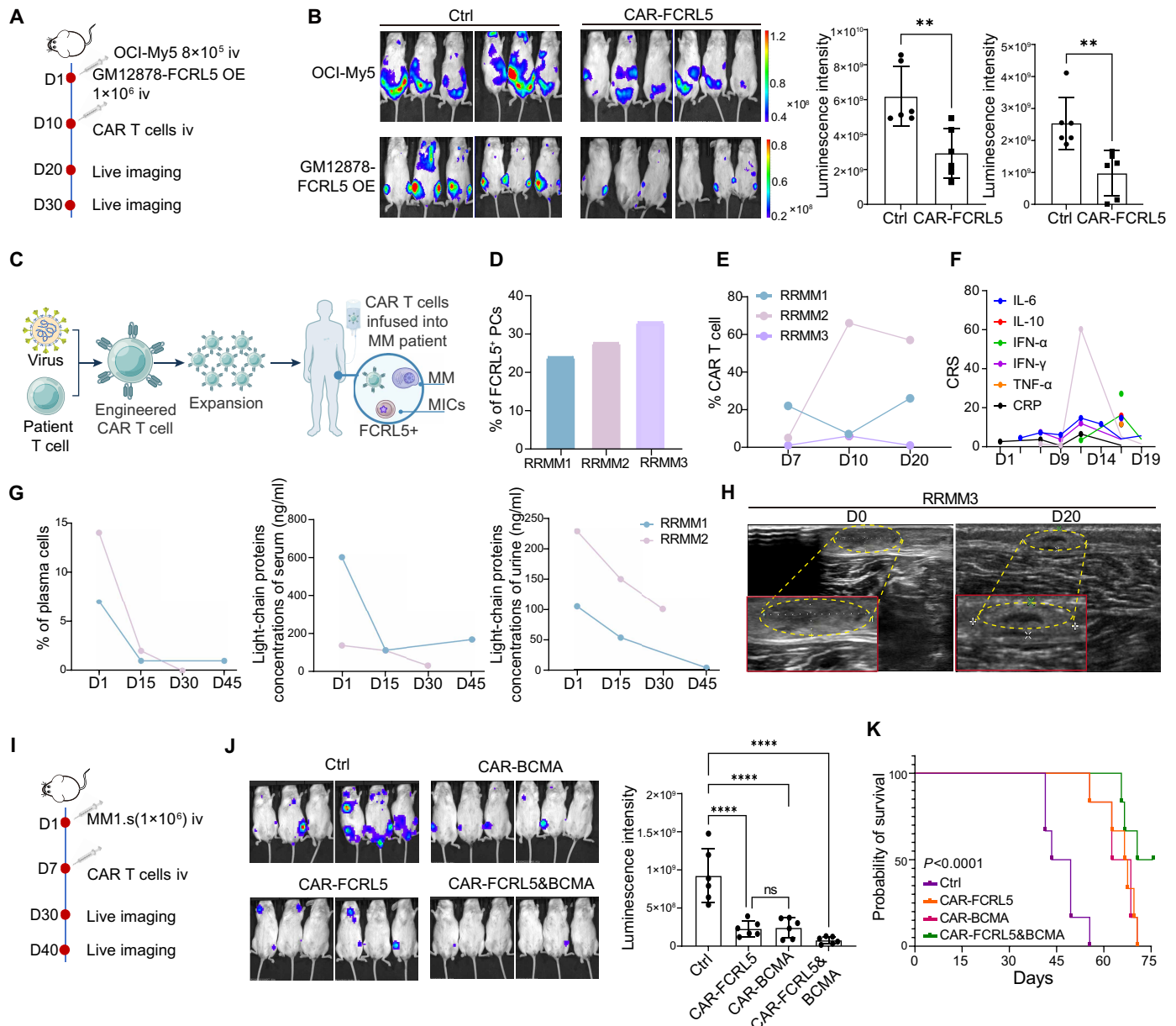


Fig. 7. Targeted FCRL5 CAR T cells in patients with RRMM achieve high safety and efficacy. (A) Schematics of the MM mouse model for antitumor efficacy of FCRL5 CAR T cells in B-NDG mice. Each OCY-My5 mouse received an injection of 8×10^5 cells, whereas in the B cell mouse model, each mouse was administered an injection of 1×10^6 GM12878-FCRL5 OE cells. iv, intravenously. (B) Live imaging and quantification of the tumor-associated luminescence intensity in B-NDG with mock T group (Ctrl) and treated with CAR-FCRL5 groups at day 20. Data are presented as the means \pm SD; n = 6; two-tailed Student's t test; **P < 0.01. (C) Schematics of phase 1 clinical trial of FCRL5 CAR T cell therapy in treating patients with MM. (D) Flow cytometry analysis of FCRL5 expression in BCs of three patients with RRMM before CART cell infusion. (E) Percentage of CAR⁺ cells among the peripheral blood T cells of patients on the indicated days before and after infusion from flow cytometry. (F) Detection of cytokine release syndrome (CRS) in patients after CAR T cell infusion by enzyme-linked immunosorbent assay, including IL-6 (IL-10), interferon- α (IFN- α), IFN- γ , tumor necrosis factor- α (TNF- α), and complement-reactive protein (CRP). (G) Proportion of free light chains and PCs from flow cytometry in RRMM1 and RRMM2. (H) B-ultrasonic scans of patient RRMM3 before and after treatment; yellow circles indicate tumor lesions. (I) Schematics of the MM.1s MM mouse model for the antitumor efficacy of FCRL5 and BCMA CART cells in B-NDG mice. (J) Live imaging in B-NDG with mock T group (Ctrl) or treated with CAR-FCRL5, CAR-BCMA, or CAR-FCRL5&BCMA (right). Data are presented as the means \pm SD; n = 6; one-way ANOVA and Tukey's test; ****P < 0.0001. (K) Survival curves of Ctrl or treated with CAR-FCRL5, CAR-BCMA, or CAR-FCRL5&BCMA groups based on (J). n = 6; log-rank (Mantel-Cox) test; ****P < 0.0001.

and BCR profiling revealed varying proportions of these biomarkers. Thus, when verifying the role and function of the BC MICs in MM malignancy, we should consider the following three factors: (i) the BC MIC subpopulation carries the unique 1q^{Amp} genetic feature of

MM cells (validated by FISH); (ii) this population demonstrates the ability to self-renew and differentiate, particularly toward PC tumors (validated by continuous cloning in vitro and tumor formation in vivo); (iii) the BCR diversity unique to BC function indicates that

the subsequently differentiated malignant PCs are monoclonally derived from the BC MIC subpopulation (validated by BCR-seq). By sorting the CD24⁻FCRL5⁺ subpopulation from specimens of patients with 1q^{Amp} MM, we confirmed that the 1q^{Amp} BC MIC subpopulation primarily induces MM malignancy through BC proliferation and PC differentiation.

This comprehensive approach allows for a nuanced understanding of tumor initiation with different genetic hits and heterogeneity (13). Furthermore, these methods highlight distinct impacts at different stages of tumor progression, especially between BCs and PCs, challenging traditional views of PC stages in MM initiation and progression. For genetic events occurring at the BC stage (for example, 1q^{Amp}), we recommend tracking whether the BC stage harbors the 1q^{Amp} BC MIC subpopulation to achieve early warning and efficacy prediction by detecting the proportion of CD24⁻FCRL5⁺ BC subsets and exploring the correlation between the proportion of initial BC subsets before and after treatment. Furthermore, the differentiation of HSCs into lymphoid cells is a tightly regulated and systematic process in which proliferation and differentiation are intricately balanced and mutually constrained. If oncogenes, such as c-Myc and Bcl2, are aberrantly activated at the BC stage without the concurrent expression of PC differentiation-associated genes, this imbalance can lead to lymphoma (41, 42). Furthermore, our study reveals that when oncogene activation occurs alongside differentiation, it can drive both the proliferation and differentiation of BCs, contributing to the malignant transformation observed in MM. Last, initiatives stemming from disrupted HSC lymphoid lineage equilibrium, MIC identification, and target gene screening may establish a multigene, multistage, multi-step clonal evolution model for MM development.

MM is still an incurable hematological malignancy. A major reason for treatment failure is the existence of a premalignant clone (MICs) or drug-resistant subclone (43), either presented at diagnosis or developed during treatment. However, current MM treatments are not suitable for targeting MICs (44). Proteasome inhibitors such as bortezomib target mature PCs, and the target of anti-CD38 monoclonal antibodies is not expressed on initiating cells. Although BCMA-targeted (32) and GPRC5D-targeted (33) CAR T cell therapies are effective in some patients, these surface markers are also not expressed on initiating cells. Thus, moving the treatment window forward is crucial. The effectiveness of CD19- and BCMA-targeted CAR T cell therapies (45) in clinical settings has greatly increased the confidence of clinical and basic researchers in BC-targeted treatments. However, patient relapses after treatment have led to new considerations. On the basis of our preclinical treatment of three patients with RRMM, all patients achieved partial remission during the period of 1 month, indicating that FCRL5 CAR T cells demonstrate high safety and efficacy for patients with MM. To this end, we will conduct a nonrandomized, open-label, single-arm phase 1 clinical study on FCRL5 CAR T cell therapy combined with anti-PC therapy, which includes first-line patients with MM who are not suitable for autologous hematopoietic stem cell transplantation and have achieved very good partial response or higher after induction therapy. The study aims to evaluate the safety of FCRL5 CAR T cell therapy; investigate pharmacokinetics, pharmacodynamics, and immunogenicity; and preliminarily evaluate its efficacy.

Our study has some limitations. We reported the treatment outcomes for only three patients with RRMM, indicating that a more comprehensive evaluation of the treatment's effectiveness necessitates a larger sample size from clinical trials. When combined with

existing therapeutic targets aimed at PCs, such as BCMA combination therapy, our animal experiment results suggested the potential for improved efficacy. Third, the underlying mechanisms contributing to the emergence of CD24⁻FCRL5⁺ BC subsets should be explored further. Future directions include expanding genetic screening and functional validation across different patient populations and refining treatment strategies, particularly for monoclonal gammopathy of undetermined significance (MM precancerous) and patients with MM who are resistant to conventional therapies. Given that FCRL5 serves as a marker for age-related BCs, future investigations should determine whether the presence of CD24⁻FCRL5⁺ BC subsets is linked to the characterization of MM as a geriatric disease.

MATERIALS AND METHODS

Study design

The aim of this study was to identify potential subgroups of MICs during the differentiation process from HSCs to PCs, as well as to identify potential therapeutic targets for MM treatment. scRNA-seq analysis, which included HSCs, BCs, and PCs from HDs and patients with NDMM, was performed to observe aberrant lymphoid lineage differentiation of HSCs in patients with MM. Genetic tracing was carried out to elucidate the origin of MICs. CNV analysis demonstrated the presence of 1q^{Amp} in BCs, which was confirmed by FISH. BCR-seq analysis of CD24⁺FCRL5⁻ and CD24⁻FCRL5⁺ BCs and PCs from the BM of patients with 1q^{Amp} MM suggested that the CD24⁻FCRL5⁺ BC subset may be the origin cell of malignant PCs in MM. Both *in vitro* and *in vivo* functional assays were conducted to assess the malignant transformation potential of CD24⁻FCRL5⁺ BC subgroups. *In vitro* validation involved sphere formation assays and PC induction differentiation experiments, whereas *in vivo* experiments used an adoptive BC transplantation model. Preclinical *in vitro* and *in vivo* functional assays were also performed to evaluate the therapeutic efficacy of CAR T cell therapy targeting FCRL5. A clinical trial was designed to assess the efficacy and safety of CAR-FCRL5 in the treatment of RRMM (ClinicalTrials.gov, NCT06196255). Patient characteristics are presented in table S6. The mice were assigned randomly to the experimental groups *in vivo*, and experiments were not performed in a blinded fashion. All experiments were typically carried out using more than three biological repeats and in three independent experiments.

Statistics

Unless otherwise specified, all statistical analyses were performed using GraphPad Prism 9. All data are expressed as the means \pm SD from at least three independent experiments. To compare differences between two groups, an unpaired Student's *t* test was performed, whereas for comparisons involving more than two groups, a one-way analysis of variance (ANOVA) was conducted. A paired *t* test was performed to compare cell subpopulations in pretreatment and posttreatment samples from the same patient source, and clinical features were analyzed using a chi-square test. Survival curves were calculated using the Kaplan-Meier method, and *P* values were determined using the log-rank test. Statistical significance was set at *P* < 0.05, and all statistical tests were two-tailed. **P* < 0.05, ***P* < 0.01, and ****P* < 0.001. The number of samples included per group is shown in each figure. The code for analysis and processed data are deposited in Zenodo at <https://doi.org/10.5281/zenodo.17222457>.

Supplementary Materials

The PDF file includes:

Materials and Methods

Figs. S1 to S12

References (46–52)

Other Supplementary Material for this manuscript includes the following:

Data S1 and S2

MDAR Reproducibility Checklist

REFERENCES AND NOTES

1. N. van de Donk, C. Pawlyn, K. L. Yong, Multiple myeloma. *Lancet* **397**, 410–427 (2021).
2. Z. Liu, X. Xu, K. Liu, J. Zhang, D. Ding, R. Fu, Immunogenic cell death in hematological malignancy therapy. *Adv. Sci.* **10**, e2207475 (2023).
3. H. Parikh, S. Lonial, Chimeric antigen receptor T-cell therapy in multiple myeloma: A comprehensive review of current data and implications for clinical practice. *CA Cancer J. Clin.* **73**, 275–285 (2023).
4. S. Leong, H. P. J. Lam, Z. Kirkham, R. Popat, Antibody drug conjugates for the treatment of multiple myeloma. *Am. J. Hematol.* **98** (Suppl. 2), S22–S34 (2023).
5. A. J. Cowan, D. J. Green, M. Kwok, S. Lee, D. G. Coffey, L. A. Holmberg, S. Tuazon, A. K. Gopal, E. N. Libby, Diagnosis and management of multiple myeloma: A review. *JAMA* **327**, 464–477 (2022).
6. F. Malard, P. Neri, N. J. Bahlis, E. Terpos, N. Moukalled, V. T. M. Hungria, S. Manier, M. Mohty, Multiple myeloma. *Nat. Rev. Dis. Primers* **10**, 45 (2024).
7. W. Zhou, Y. Yang, J. Xia, H. Wang, M. E. Salama, W. Xiong, H. Xu, S. Shetty, T. Chen, Z. Zeng, L. Shi, M. Zangari, R. Miles, D. Bearss, G. Tricot, F. Zhan, NEK2 induces drug resistance mainly through activation of efflux drug pumps and is associated with poor prognosis in myeloma and other cancers. *Cancer Cell* **23**, 48–62 (2013).
8. X. Feng, J. Guo, G. An, Y. Wu, Z. Liu, B. Meng, N. He, X. Zhao, S. Chen, Y. Zhu, J. Xia, X. Li, Z. Yu, R. Li, G. Ren, J. Chen, M. Wu, Y. He, L. Qiu, J. Zhou, W. Zhou, Genetic aberrations and interaction of NEK2 and TP53 accelerate aggressiveness of multiple myeloma. *Adv. Sci.* **9**, e2104491 (2022).
9. C. Kuang, M. Xia, G. An, C. Liu, C. Hu, J. Zhang, Z. Liu, B. Meng, P. Su, J. Xia, J. Guo, Y. Zhu, X. Liu, X. Wu, Y. Shen, X. Feng, Y. He, J. Li, L. Qiu, J. Zhou, W. Zhou, Excessive serine from the bone marrow microenvironment impairs megakaryopoiesis and thrombopoiesis in multiple myeloma. *Nat. Commun.* **14**, 2093 (2023).
10. J. Xia, J. Zhang, X. Wu, W. Du, Y. Zhu, X. Liu, Z. Liu, B. Meng, J. Guo, Q. Yang, Y. Wang, Q. Wang, X. Feng, G. Xie, Y. Shen, Y. He, J. Xiang, M. Wu, G. An, L. Qiu, W. Jia, W. Zhou, Blocking glycine utilization inhibits multiple myeloma progression by disrupting glutathione balance. *Nat. Commun.* **13**, 4007 (2022).
11. Y. Zhu, X. Jian, S. Chen, G. An, D. Jiang, Q. Yang, J. Zhang, J. Hu, Y. Qiu, X. Feng, J. Guo, X. Chen, Z. Li, R. Zhou, C. Hu, N. He, F. Shi, S. Huang, H. Liu, X. Li, L. Xie, Y. Zhu, L. Zhao, Y. Jiang, J. Li, J. Wang, L. Qiu, X. Chen, W. Jia, Y. He, W. Zhou, Targeting gut microbial nitrogen recycling and cellular uptake of ammonium to improve bortezomib resistance in multiple myeloma. *Cell Metab.* **36**, 159–175.e8 (2024).
12. D. Hanahan, Hallmarks of cancer: New dimensions. *Cancer Discov.* **12**, 31–46 (2022).
13. J. E. Visvader, Cells of origin in cancer. *Nature* **469**, 314–322 (2011).
14. A. K. Dutta, J. B. Alberge, R. Sklavenitis-Pistofidis, E. D. Lightbody, G. Getz, I. M. Ghobrial, Single-cell profiling of tumour evolution in multiple myeloma—Opportunities for precision medicine. *Nat. Rev. Clin. Oncol.* **19**, 223–236 (2022).
15. W. Matsui, C. A. Huff, Q. Wang, M. T. Malehorn, J. Barber, Y. Tanhehco, B. D. Smith, C. I. Civin, R. J. Jones, Characterization of clonogenic multiple myeloma cells. *Blood* **103**, 2332–2336 (2004).
16. W. Matsui, Q. Wang, J. P. Barber, S. Brennan, B. D. Smith, I. Corrello, I. McNiece, L. Lin, R. F. Ambinder, C. Peacock, D. N. Watkins, C. A. Huff, R. J. Jones, Clonogenic multiple myeloma progenitors, stem cell properties, and drug resistance. *Cancer Res.* **68**, 190–197 (2008).
17. C. Vicente-Duenas, I. Romero-Camarero, I. Gonzalez-Herrero, E. Alonso-Escudero, F. Abollo-Jimenez, X. Jiang, N. C. Gutierrez, A. Orfao, N. Marin, L. M. Villar, M. C. Criado, B. Pintado, T. Flores, D. Alonso-Lopez, J. De Las Rivas, R. Jimenez, F. J. Criado, M. B. Cenador, I. S. Lossos, C. Cobaleda, I. Sanchez-Garcia, A novel molecular mechanism involved in multiple myeloma development revealed by targeting MafB to haematopoietic progenitors. *EMBO J.* **31**, 3704–3717 (2012).
18. S. Yaccobi, J. Epstein, The proliferative potential of myeloma plasma cells manifest in the SCID-hu host. *Blood* **94**, 3576–3582 (1999).
19. M. Shapiro-Shelef, K. Calame, Regulation of plasma-cell development. *Nat. Rev. Immunol.* **5**, 230–242 (2005).
20. W. Wei, Y. S. Shin, M. Xue, T. Matsutani, K. Masui, H. Yang, S. Ikegami, Y. Gu, K. Herrmann, D. Johnson, X. Ding, K. Hwang, J. Kim, J. Zhou, Y. Su, X. Li, B. Bonetti, R. Chopra, C. D. James, W. K. Cavenee, T. F. Cloughesy, P. S. Mischel, J. R. Heath, B. Gini, Single-cell phosphoproteomics resolves adaptive signaling dynamics and informs targeted combination therapy in glioblastoma. *Cancer Cell* **29**, 563–573 (2016).
21. X. Xiang, Y. He, Z. Zhang, X. Yang, Interrogations of single-cell RNA splicing landscapes with SCASL define new cell identities with physiological relevance. *Nat. Commun.* **15**, 2164 (2024).
22. Y. Zhang, X. Xie, Y. Huang, M. Liu, Q. Li, J. Luo, Y. He, X. Yin, S. Ma, W. Cao, S. Chen, J. Peng, J. Guo, W. Zhou, H. Luo, F. Dong, H. Cheng, S. Hao, L. Hu, P. Zhu, T. Cheng, Temporal molecular program of human hematopoietic stem and progenitor cells after birth. *Dev. Cell* **57**, 2745–2760.e6 (2022).
23. T. Stuart, A. Butler, P. Hoffman, C. Hafemeister, E. Papalexi, W. M. Mauck III, Y. Hao, M. Stoeckius, P. Smibert, R. Satija, Comprehensive integration of single-cell data. *Cell* **177**, 1888–1902.e21 (2019).
24. S. C. Bendall, K. L. Davis, E.-A. D. Amir, M. D. Tadmor, E. F. Simonds, T. J. Chen, D. K. Shenfeld, G. P. Nolan, D. Pe'er, Single-cell trajectory detection uncovers progression and regulatory coordination in human B cell development. *Cell* **157**, 714–725 (2014).
25. L. Alberti-Servera, L. von Muenchow, P. Tsapogas, G. Capoferra, K. Eschbach, C. Beisel, R. Ceredig, R. Ivanek, A. Rolink, Single-cell RNA sequencing reveals developmental heterogeneity among early lymphoid progenitors. *EMBO J.* **36**, 3619–3633 (2017).
26. M. Dang, R. Wang, H. C. Lee, K. K. Patel, M. R. Becnel, G. Han, S. K. Thomas, D. Hao, Y. Chu, D. M. Weber, P. Lin, Z. Lutter-Berka, D. A. Berrios Nolasco, M. Huang, H. Bansal, X. Song, J. Zhang, A. Futreal, L. Y. Moreno Rueda, D. E. Symer, M. R. Green, C. M. Rojas Hernandez, M. Kroll, V. Afshar-Khargan, L. J. Ndacyasaba, P. Kuhn, S. S. Neelapu, R. Z. Orlowski, L. Wang, E. E. Manasanch, Single cell clonotypic and transcriptional evolution of multiple myeloma precursor disease. *Cancer Cell* **41**, 1032–1047.e4 (2023).
27. O. Zavidij, N. J. Hardhvala, T. H. Mouhieddine, R. Sklavenitis-Pistofidis, S. Cai, M. Reidy, M. Rahmat, A. Flaifel, B. Ferland, N. K. Su, M. P. Agius, J. Park, S. Manier, M. Bustoros, D. Huynh, M. Capellotti, B. Berrios, C. J. Liu, M. X. He, E. Braggio, R. Fonseca, Y. E. Maruvka, J. L. Guerrero, M. Goldman, E. M. Van Allen, S. A. McCarroll, J. Azzi, G. Getz, I. M. Ghobrial, Single-cell RNA sequencing reveals compromised immune microenvironment in precursor stages of multiple myeloma. *Nat. Cancer* **1**, 493–506 (2020).
28. S. M. Tirier, J. P. Mallm, S. Steiger, A. M. Poos, M. H. S. Awwad, N. Giesen, N. Casiraghi, H. Susak, B. Bauer, A. Baumann, L. John, A. Seckinger, D. Hose, C. Muller-Tidow, H. Goldschmidt, O. Stegle, M. Hundemer, N. Weinhold, M. S. Raab, K. Rippe, Subclone-specific microenvironmental impact and drug response in refractory multiple myeloma revealed by single-cell transcriptomics. *Nat. Commun.* **12**, 6960 (2021).
29. X. Qiu, Y. Zhang, J. D. Martin-Rufino, C. Weng, S. Hosseini-zadeh, D. Yang, A. N. Pogson, M. Y. Hein, K. H. J. Min, L. Wang, E. I. Grody, M. J. Shurtliff, R. Yuan, S. Xu, Y. Ma, J. M. Replogle, E. S. Lander, S. Darmanis, I. Bahar, V. G. Sankaran, J. Xing, J. S. Weissman, Mapping transcriptomic vector fields of single cells. *Cell* **185**, 690–711.e45 (2022).
30. G. La Manno, R. Soldatov, A. Zeisel, E. Braun, H. Hochgerter, V. Petukhov, K. Lidschreiber, M. E. Kastriti, P. Lonnerberg, A. Furlan, J. Fan, L. E. Borm, Z. Liu, D. van Bruggen, J. Guo, X. He, R. Barker, E. Sundstrom, G. Castelo-Branco, P. Cramer, I. Adameyko, S. Linnarsson, P. V. Kharchenko, RNA velocity of single cells. *Nature* **560**, 494–498 (2018).
31. K. Rycaj, D. G. Tang, Cell-of-origin of cancer versus cancer stem cells: Assays and interpretations. *Cancer Res.* **75**, 4003–4011 (2015).
32. B. Yu, T. Jiang, D. Liu, BCMA-targeted immunotherapy for multiple myeloma. *J. Hematol. Oncol.* **13**, 125 (2020).
33. S. Mailankody, S. M. Devlin, J. Landa, K. Nath, C. Diamonte, E. J. Carstens, D. Russo, R. Auclair, L. Fitzgerald, B. Cadzin, X. Wang, D. Sikder, B. Senechal, V. P. Bermudez, T. J. Purdon, K. Hosszu, D. P. McAvoy, T. Farzana, E. Mead, J. A. Wilcox, B. D. Santomasso, G. L. Shah, U. A. Shah, N. Korde, A. Lesokhin, C. R. Tan, M. Hultcrantz, H. Hassoun, M. Roshal, F. Sen, A. Dogan, O. Landgren, S. A. Giralt, J. H. Park, S. Z. Usmani, I. Riviere, R. J. Brentjens, E. L. Smith, GPRC5D-targeted CAR T cells for myeloma. *N. Engl. J. Med.* **387**, 1196–1206 (2022).
34. D. Dai, S. Gu, X. Han, H. Ding, Y. Jiang, X. Zhang, C. Yao, S. Hong, J. Zhang, Y. Shen, G. Hou, B. Qu, H. Zhou, Y. Qin, Y. He, J. Ma, Z. Yin, Z. Ye, J. Qian, Q. Jiang, L. Wu, Q. Guo, S. Chen, C. Huang, L. C. Kotyan, M. T. Weirauch, C. G. Vinuesa, N. Shen, The transcription factor ZEB2 drives the formation of age-associated B cells. *Science* **383**, 413–421 (2024).
35. M. P. Cancro, Age-associated B cells. *Annu. Rev. Immunol.* **38**, 315–340 (2020).
36. Y. Hu, M. Zheng, R. Gallo, Z. Tian, G. Topal Görgün, N. C. Munshi, C. S. Mitsiades, K. C. Anderson, A novel rapid-onset high-penetrance plasmacytoma mouse model driven by deregulation of cMYC cooperating with KRAS12V in BALB/c mice. *Blood Cancer J.* **3**, e156 (2013).
37. C. R. Escalante, A. L. Brass, J. M. Pongubala, E. Shatova, L. Shen, H. Singh, A. K. Aggarwal, Crystal structure of PU.1/IRF-4/DNA ternary complex. *Mol. Cell* **10**, 1097–1105 (2002).
38. M. Busslinger, Transcriptional control of early B cell development. *Annu. Rev. Immunol.* **22**, 55–79 (2004).
39. J. Li, N. J. Stagg, J. Johnston, M. J. Harris, S. A. Menzies, D. DiCara, V. Clark, M. Hristopoulos, R. Cook, D. Slaga, R. Nakamura, L. McCarty, S. Sukumaran, E. Luis, Z. Ye, T. D. Wu, T. Sumiyoshi, D. Danilenko, G. Y. Lee, K. Totpal, D. Ellerman, I. Hotzel, J. R. James, T. T. Junntila, Membrane-proximal epitope facilitates efficient T cell synapse formation by anti-FcRH5/CD3 and is a requirement for myeloma cell killing. *Cancer Cell* **31**, 383–395 (2017).

40. R. J. Gilbertson, Mapping cancer origins. *Cell* **145**, 25–29 (2011).
41. J. P. Castro, A. V. Shindyapina, A. Barbieri, K. Ying, O. S. Strelkova, J. A. Paulo, A. Tyshkovskiy, R. Meinl, C. Kerepesi, A. P. Petrashev, M. Mariotti, M. V. Meer, Y. Hu, A. Karamyshev, G. Losyev, M. Galhardo, E. Logarinho, A. A. Indzhykulian, S. P. Gygi, J. M. Sedivy, J. P. Manis, V. N. Gladyshev, Age-associated clonal B cells drive B cell lymphoma in mice. *Nat. Aging* **4**, 1403–1417 (2024).
42. L. Pasqualucci, M. Compagno, J. Houldsworth, S. Monti, A. Grunn, S. V. Nandula, J. C. Aster, V. V. Murty, M. A. Shipp, R. Dalla-Favera, Inactivation of the PRDM1/BLIMP1 gene in diffuse large B cell lymphoma. *J. Exp. Med.* **203**, 311–317 (2006).
43. M. K. Samur, R. Szalat, N. C. Munshi, Single-cell profiling in multiple myeloma: Insights, problems, and promises. *Blood* **142**, 313–324 (2023).
44. S. V. Rajkumar, Multiple myeloma: 2020 update on diagnosis, risk-stratification and management. *Am. J. Hematol.* **95**, 548–567 (2020).
45. W. Wang, S. He, W. Zhang, H. Zhang, V. M. DeStefano, M. Wada, K. Pinz, G. Deener, D. Shah, N. Hagag, M. Wang, M. Hong, R. Zeng, T. Lan, Y. Ma, F. Li, Y. Liang, Z. Guo, C. Zou, M. Wang, L. Ding, Y. Ma, Y. Yuan, BCMA-CD19 compound CAR T cells for systemic lupus erythematosus: A phase 1 open-label clinical trial. *Ann. Rheum. Dis.* **83**, 1304–1314 (2024).
46. Y. Hao, S. Hao, E. Andersen-Nissen, W. M. Mauck III, S. Zheng, A. Butler, M. J. Lee, A. J. Wilk, C. Darby, M. Zager, P. Hoffman, M. Stoeckius, E. Papalexi, E. P. Mimitou, J. Jain, A. Srivastava, T. Stuart, L. M. Fleming, B. Yeung, A. J. Rogers, J. M. McElrath, C. A. Blish, R. Gottardo, P. Smibert, R. Satija, Integrated analysis of multimodal single-cell data. *Cell* **184**, 3573–3587.e29 (2021).
47. M. Kang, J. J. A. Armenteros, G. S. Gulati, R. Gleyzer, S. Avagyan, E. L. Brown, W. Zhang, A. Usmani, N. Earland, Z. Wu, J. Zou, R. C. Fields, D. Y. Chen, A. A. Chaudhuri, A. M. Newman, Mapping single-cell developmental potential in health and disease with interpretable deep learning. *bioRxiv* 585637 [Preprint] (2024). <https://doi.org/10.1101/2024.03.19.585637>.
48. J. Cao, M. Spielmann, X. Qiu, X. Huang, D. M. Ibrahim, A. J. Hill, F. Zhang, S. Mundlos, L. Christiansen, F. J. Steemers, C. Trapnell, J. Shendure, The single-cell transcriptional landscape of mammalian organogenesis. *Nature* **566**, 496–502 (2019).
49. K. Street, D. Risso, R. B. Fletcher, D. Das, J. Ngai, N. Yosef, E. Purdom, S. Dudoit, Slingshot: Cell lineage and pseudotime inference for single-cell transcriptomics. *BMC Genomics* **19**, 477 (2018).
50. J. M. Granja, M. R. Corces, S. E. Pierce, S. T. Bagdatli, H. Choudhry, H. Y. Chang, W. J. Greenleaf, ArchR is a scalable software package for integrative single-cell chromatin accessibility analysis. *Nat. Genet.* **53**, 403–411 (2021).
51. S. Aibar, C. B. Gonzalez-Blas, T. Moerman, V. A. Huynh-Thu, H. Imrichova, G. Hulselmans, F. Rambow, J. C. Marine, P. Geurts, J. Aerts, J. van den Oord, Z. K. Atak, J. Wouters, S. Aerts, SCENIC: Single-cell regulatory network inference and clustering. *Nat. Methods* **14**, 1083–1086 (2017).
52. J. Wu, K. Yang, S. Cai, X. Zhang, L. Hu, F. Lin, S. Q. Wu, C. Xiao, W. H. Liu, J. Han, A p38 α -BLIMP1 signalling pathway is essential for plasma cell differentiation. *Nat. Commun.* **13**, 7321 (2022).

Acknowledgments: We thank P. Zhu from the State Key Laboratory of Experimental Hematology for technical support. We appreciate the mice and cells gifted by J. Wu, B. Leif, and C. Li. We thank the Animal Center of Hunan Normal University and School of Medicine and Biomedical Center, Institute for Advanced Study of Central South University for providing the experimental platform. **Funding:** This work was supported by the National Natural Science Foundation of China 82430008 and 82108006 to W.Z., 82300237 to J.G., and 62422318 and 62173338 to H.C.; National Key Research and Development Program of China 2023YFF0725500 to H.C.; the Scientific Research Program of Furong Laboratory 2024PT5109 to J.G.; National Natural Science Foundation of Hunan Province 2024JJ6655 to J.G.; and State Key Laboratory of Medical Proteomics SKLP-K202407 to H.C. **Author contributions:** W.Z. and T.C. provided the idea of the paper; W.Z., J.G., and Q.L. designed the experiments; Z.Y. and K.X. designed and conducted clinical trials; H.C., Y.L., Z. Liu, and L.X. performed bioinformatics analyses; W.Z., H.C., and J.G. provided funding; Q.L., F.S., X.W., J.Y., and S.H. conducted single-cell sorting and library construction; Z. Li, R.Z., and N.H. created the mouse model; J.Z. and W.J. provided technical and instrument equipment assistance; J.G., Y.Z., X.C., F.S., and X.F. performed molecular biology experiments; L.Z., Y.Q., Y.H., G.A., and J.L. collected surgical specimens and clinical data; W.Z., J.G., Y.L., and Q.L. wrote the manuscript; and H.C., K.X., T.C., X.B., and Z.Y. reviewed and edited the manuscript. **Competing interests:** This article has an ongoing patent application (co-inventors: W.Z., J.G., Y.L., H.C., and K.X.; patent title: "The markers of 1q amplified multiple myeloma and their applications and detection formulations"; no. 2025110652851). The other authors declare that they have no competing interests.

Data and materials availability: All data associated with this study are present in the paper or the Supplementary Materials. The raw sequence data reported in this paper have been deposited in the Genome Sequence Archive in National Genomics Data Center, China National Center for Bioinformation/Beijing Institute of Genomics, Chinese Academy of Sciences (HRA007007), the expression matrix has been uploaded to Zenodo (<https://doi.org/10.5281/zenodo.17222457>). Public scRNA-seq datasets used in this study were from European Genome-Phenome Archive (EGA; accession number: EGAS00001006694) and Gene Expression Omnibus (GEO; accession numbers: GSE137864, GSE128639, GSE124310, and GSE161801), and ChIP-seq datasets were from ENCODE.

Submitted 22 October 2024

Resubmitted 24 April 2025

Accepted 29 October 2025

Published 19 November 2025

10.1126/scitranslmed.adu0114